# Chapter 1   Introduction

## 1.1   Microdisk, Microgear, and Microflower

The microdisk is firstly proposed by S. L. McCall *et al* in 1991 [1], which is composed by a thin semiconductor disk consists of multi quantum wells (MQWs) as shown in Fig. 1.1 (a). By total internal reflection (TIR) due to the index contrast between air and the disk, light will be well confined in the disk region.

The main resonance mode in microdisk is the whispering gallery (WG) mode, which is named after whispering gallery by St. Paul's Cathedral in London. As shown in Fig. 2 (a), the WG mode is formed by a series of TIRs along the circumference of disk, and the light will form a periodic standing wave with specific wavelength. The WG mode is specified by the lobes of standing wave. For example, the $WG_{6,1}$ mode shown in Fig. 1.2 (b) is the target mode we will investigate in this thesis, where the former sub-number denotes the azimuthal number and the latter one denotes the order of radial mode.

So far, because of its advantages such as high quality (Q) factor, low threshold, and spontaneous emission control, microdisk has long been regarded as the potential microcavity for various applications, including semiconductor lasers [2], optical sensors [3], filters [4], and so on.

(a)   (b)
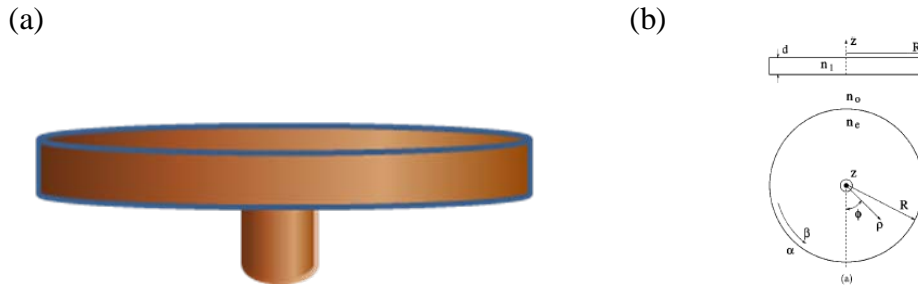
Fig. 1.1   (a) The scheme of microdisk composed by thin semiconductor disk. (b) The

scheme of total internal reflection in microdisk.
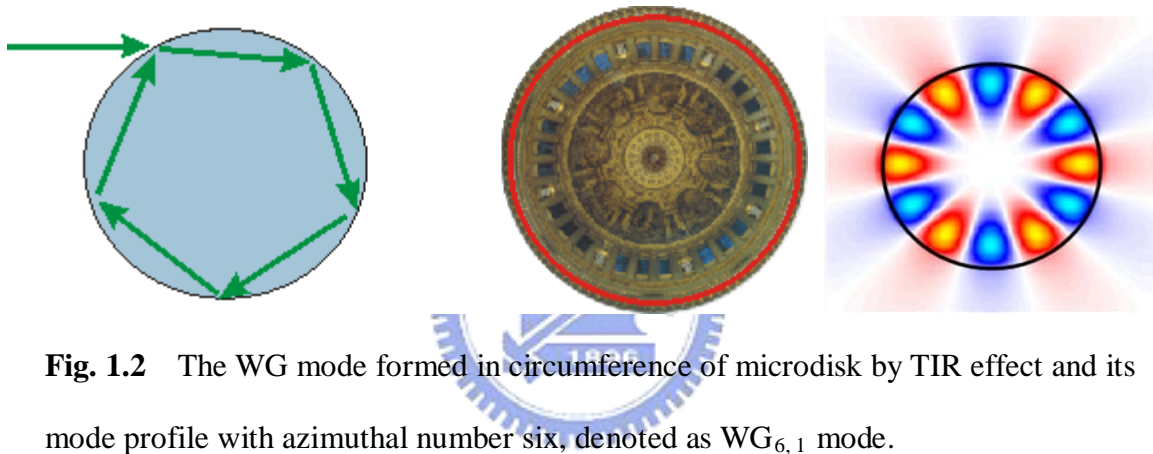

Fig. 1.2   The WG mode formed in circumference of microdisk by TIR effect and its

mode profile with azimuthal number six, denoted as $\text{WG}_{6,1}$ mode.

However, since the main confinement mechanism of microdisk is the TIR effect, when

the cavity size is shrunk to wavelength scale, the ability of confinement will dramatically

drop due to the increased bend loss caused by smaller disk radius. When the optical loss

increases, the laser performance including Q factor and threshold will be degraded. For

example, when the microdisk size is very large, the Q factor of WG mode can even be as high

as several billion [5,6]. But when the disk size is reduced to be wavelength scale, for example,

$\text{WG}_{6,1}$ mode in microdisk with 0.9 μ m in radius, the Q factor will only be about 700.

In microdisk related researches, although the basic limitation of TIR cannot be broken, researches can still optimize the degraded laser performance by various designs. In 2001, M. Fujita and T. Baba firstly proposed the concept of micro-gears [7] as shown in Fig. 1.3 (a). The scanning electron microscope picture of fabricated device is also shown in Fig. 1.3 (b). As one can see from Fig. 1.3, the periodic gratings (micro-gears) are formed at circumference of the microcavity. The micro-gears play two key roles in optimized the degraded lasing performance. First, the bend loss will be reduced due to the elongated circumference length. Second, the other WG modes with azimuthal number mismatch with grating periods will be greatly suppressed. This can reduce the un-necessary carrier contribute to the non-lasing mode and the threshold will decrease.

Furthermore, according to the concept mentioned above, it is reasonable and naturally to further modify the micro-gears more "smooth", that is, more matching with the WG mode profile. And then the micro-flower is proposed. The scheme of micro-flower with radius of 0.9 ìm is also shown in Fig. 3 (c).
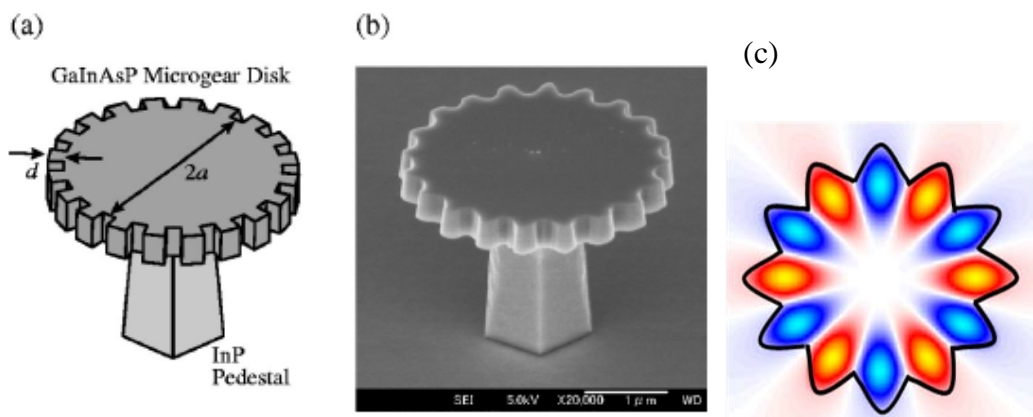

Fig. 1.3 (a) Scheme and (b) its SEM picture of microdisk laser with microgear proposed by M. Fujita, and T. Baba. (Adopted from Masayuki Fujita and Toshihiko BaBa) (c) The scheme of micro-flower with radius of 0.9 um.

Although lots great ideas have been proposed and investigated, the basic limitation of TIR confinement in micro-disk still cannot be broken, that is, diffraction limitation. Thus, it is impossible for us to further increase the Q factor, especially when the disk size is close to sub-wavelength scale. And this is also well-known as the largest bottleneck when minimizing the device size. To solve this bottleneck, recently, photonic crystal micro- and nano-cavities [8,9] based on photonic band-gap (PBG) effect have been widely designed, fabricated, and characterized. Various excellent lasing properties have been reported.

1.2   Photonic Crystal Microcavity

The concept of photonic crystal was first proposal by E. Yablonovitch in 1987 [10], which mean the material with periodic refractive index arrangement. This kind of material can be found in our world or fabricated artificially by our human beings technologies. According to their index periodic variation dimension, one can classify them into one- (1D), two- (2D) and three-dimensional (3D) photonic crystals, as shown in Fig. 1.4.
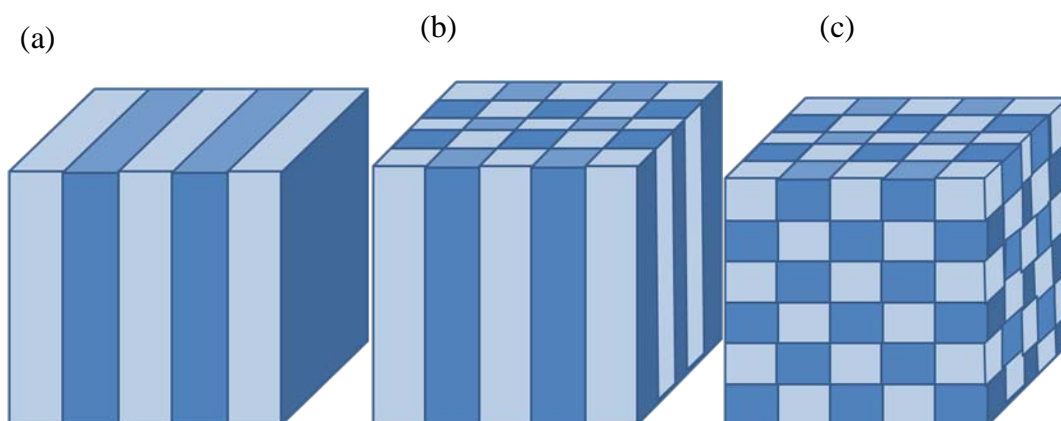
Fig. 1.4   The scheme of (a) 1D, (b) 2D, and (c) 3D photonic crystal.

The PBG effect is the most important characteristic in photonic crystal, which means the light propagation will be forbidden within certain frequency range in photonic crystal. We can understand the PBG effect from the electronic band theory in crystals. In this theory, the behavior of electron will be affected by periodic crystal structure and obey the time-independent Schrodinger equation:

$$-\frac{\hbar^2}{2m}\frac{\partial}{dx^2}+U(x)\psi(x)=E\psi(x)$$

In certain energy levels, the Ø(r) term will be equal to zero, which means that the existence probability of electron in these energy levels is zero. Then these energy levels will form the electronic band gap in electronic band structure.

The behavior of light in photonic crystals can be regarded as analog to electrons in crystal. The periodic index variations in photonic crystals for photons play the similar role as the atoms in solid crystals for electrons. Its behavior will obey the master equations from Maxwell's equations:

$$\vec{\nabla}\times\frac{1}{\varepsilon}\vec{\nabla}\times\vec{H}=\left(\frac{\omega}{c}\right)^2\vec{H}$$

Where ε is dielectric constant function depends on position and H is the magnetic field. Deriving from this equation, the H becomes exponential decay in some specific frequencies. It means that the light is forbidden propagating in these frequencies and this forbidden frequency zone is the well-known PBG region. In Fig. 1.5 (a) and (b), one can see a photonic crystal TE band diagram of the triangular lattice photonic crystals with air hole radius (r) over lattice constant (a) ratio (r/a ratio) of 0.25 and a = 1000 nm.
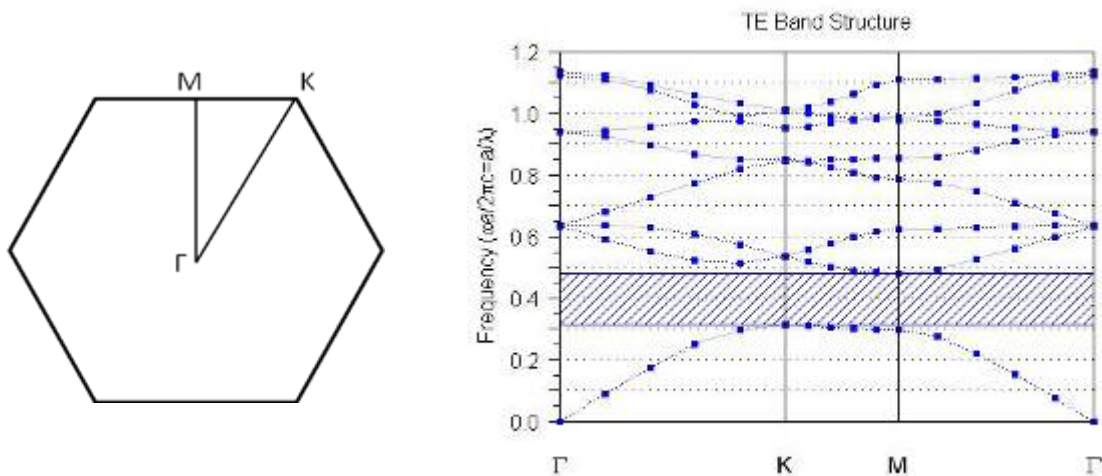
Fig. 1.5 (a) The scheme of triangular photonic crystal and its Brillioun Zone. (b) The calculated triangular photonic crystal TE mode band structure with *r/a* = 0.25 and *a* = 1000 nm.

This PBG effect also provides our human being the possibility of controlling light by inducing various defects in photonic crystal, for example, cavity and waveguides devices. The first photonic crystal microcavity laser was demonstrated by O. Painter *et al.* [11], and its scheme is shown in Fig. 6. In this structure, the photonic crystal is formed by the fabricated air holes on a thin dielectric slab with top and bottom air-cladding. The microcavity is formed by removing one or more air holes as shown in Fig. 1.6. In the microcavity, there are two different confinement mechanisms in two different directions. The vertical direction confinement is provided by the TIR effect from the index contrast of top and bottom interface. And the in-plane direction confinement is provided by PBG effect. Due to the PBG confinement without considering ray-tracing rule, the bend loss problem will not exist anymore. Thus, there will be larger *Q* factor in photonic crystal microcavity than that in micro-disks.

Total internal reflection (TIR)
Distributed Bragg reflection (DBR)

Fig. 1.6 The scheme of photonic crystal membrane microcavity.

Although lots different photonic crystal lattice structures have been proposed and investigated, triangular photonic crystal is the most widely used lattice structure. The reason is that there will be wider PBG in triangular lattice under the same r/a ratio compared with the other lattice structures. In recent years, various photonic crystal microcavity design aiming at various properties have been proposed and investigated, for example, ultra-high Q factor from hetero-structure waveguide-type and L3 microcavity [12], ultra-small mode volume from point-shifted nanocavity [13], high spontaneous emission (β) factor, and so on. However, we find that the high Q WG mode is rarely sustained in most photonic crystal microcavity designs.

The reason why we use WG mode is that there will be a significant zero-distribution region at the center of the microcavity. This means that we can insert a central post to inject current and serve as a heat sinker without affecting the lasing performance. In my thesis in chapter 3, we will introduce a photonic crystal microcavity design named CD_2 microcavity

with enhanced $WG_{6,1}$ mode according to the micro-gear topology. Besides, due to its topology design, according to the topology optimization in microdisk, we can further optimize the photonic crystal CD_2 microcavity. Although the confinement mechanisms are totally different in micro-disk and photonic crystal microcavity, investigating the topology role plays in WG mode Q factor optimization would be very interesting.

1.3   Photonic Molecules (PM)

Photonic molecule was firstly brought out by M. Bayer *et al.* in 1998, which was named after chemical molecular because of their similar behavior, that is, optical analog to bonding and anti-bonding state. The simplest and most widely-investigated PM is consisted of two identical semiconductor micro-disks sustaining high Q WG modes as shown in Fig. 1.7, which exhibits unique behaviors including filtering, switching, bistability [15,16], and so on. It also suffered from the same bottleneck as in microdisk we mentioned before. According to our previous introduction, we can also construct PMs by photonic crystal microcavities instead of microdisks. Up to date, several PMs and coupling cavities have also been proposed and reported [14], which the photonic crystal microcavities are all designed and fabricated on the single membrane, in other words, on the same plane, the same way of designing PMs composed by microdisks.
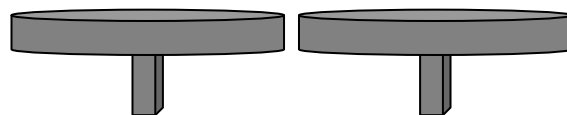

Fig. 1.7 A simple PMs constructed by two fabricated identical microdisks side by side.

However, there are two main disadvantages for photonic crystal PMs. First, in photonic crystal membrane microcavity, when the surrounded photonic crystal lattice periods are sufficiently large, the main coupling is dominated only in the vertical direction governed by TIR effect, which is very different from TIR confinement in all directions in microdisks. Thus, for PMs constructed on single photonic crystal membrane, before coupling, each cavity will suffer extra losses for individual resonance caused by the neighboring cavities, which means the in-plane PBG confinement will be weakened and the Q factors of PMs will be reduced. Second, the geometry of photonic crystal PM on single layer is strongly limited by photonic crystal lattice structure [17-20], which will limit the variable and controllable abilities of PMs integrated in PICs.

To solve the issues mentioned above, in this thesis, we propose a PM design named double-layer PM (DLPM), which is shown in Fig. 1.8, based on the photonic crystal microcavity with enhanced $WG_{6,1}$ mode in this thesis. From this design, in my thesis, we will investigate and address its PM states and its applications.
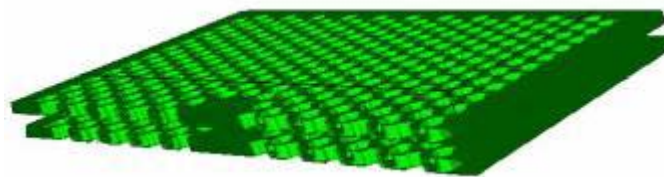
Fig. 1.8 The scheme of DLPM composed by two identical photonic crystal microcavity membranes sustaining enhanced $WG_{6,1}$ mode.

1.4 An Overview of This Thesis

In my thesis, there will be two part, the first part is research on microflower topology in microdisk and the effect when this topology transferred on photonic crystal microcavity with enhanced $WG_{6,1}$ mode we proposed in this thesis. In chapter 2, by using finite-difference time-domain (FDTD) simulations, we will investigate the Q factor optimization from micro-disk, micro-gear, to micro-flower topology. In chapter 3, at first, we will introduce and investigate a new photonic crystal microcavity design with enhanced $WG_{6,1}$ mode, including simulations, fabrications, and measurements. And then, according to the optimized micro-flower topology in chapter 2, we will apply it on the photonic crystal microcavity and find out the role it plays in optimizing Q factor of $WG_{6,1}$ mode. The second part is the brand new idea of DLPM based on the photonic crystal microcavity with WG mode in the first part. In chapter 4, the brand new idea DLPM will be verified and investigated also by using 3D FDTD simulations, including the PM states addressing, controllable Q factor, and so on. And then, the related fabrication developing based on this structure by GaAs / AlGaAs system will be also illustrated. Finnally, there will be a brief conclusion in chapter 5.

Chapter 2   From Microdisk, Microgear, to Microflower: Design and Optimization

2.1   Introduction

In this chapter, we are going to use FDTD method to investigate the WG modal properties and the Q factor improvement from micro-disk, micro-gear, in small to micro-flower topologies. In paragraph 2.2, we will introduce FDTD method applied in the following simulations. In paragraph 2.3, we will introduce the micro-disk and the micro-gear topology, including the simulation results in optimizing Q factor of WG mode and discussions. In paragraph 2.4, we will further optimize the micro-gear to be micro-flower and discuss the result of simulation. In paragraph 2.5, there will be a brief conclusion.
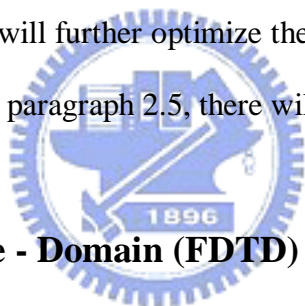
2.2   Finite-Difference Time - Domain (FDTD) Method

In the calculation of wave equation of electromagnetic field, FDTD method is the most popular computer numerical computation. It can help us to solve the ODE of Maxwell's equation. We can express the continuous Maxwell's equation in finite-difference sequence and it can reduce the time of computer operation. Time-domain can help us to simulate the single procedure in wide range of frequency. That's why we will use FDTD method when we need to handle the Maxwell's equation.

The main concept of FDTD method is to separate the transform space of continuous electromagnetic field into several small segments. In other words, FDTD method makes the time domain and space domain discretely.

At first, we make a description of discrete in time domain, as follows:

$$\frac{\partial F^n}{\partial t} = \frac{F^{n+1/2}(i,j,k) - F^{n-1/2}(i,j,k)}{\Delta t}$$

In general, we use the central difference because it has the less inaccuracy when operating with FDTD method. We can locate each point in coordinate as:

$$(i, j, k) = (i\Delta x, j\Delta y, k\Delta z)$$

By observing the configuration of time, we can find the electric field and magnetic field in electromagnetic wave will generate interactively, therefore we can get time express in time domain as:

E(n)Δt, E(n+1)Δt, ……

H(n-1/2)Δt, H(n+1/2)Δt, ……

If we want to get the electromagnetic field in next time segment by the former time segment, we can find the electric field E(n)Δt = E(n-1)Δt + H(n-1/2)Δt, and magnetic field H(n+1/2)Δt = E(n)Δt + H(n-1/2)Δt.

Then we discuss the differences in time domain, deriving from the curl of Maxwell's equation we know

$$\nabla \times E(r,t) = -\frac{\partial B(r,t)}{\partial t}$$

$$\nabla \times H(r,t) = J(r,t) + \frac{\partial D(r,t)}{\partial t}$$

And then substitute them to the equation mentioned before:

$$\frac{\partial H_x}{\partial t} = \frac{1}{\mu}\left(\frac{\partial E_x}{\partial y} - \frac{\partial E_y}{\partial x}\right)$$

$$\frac{\partial H_y}{\partial t} = \frac{1}{\mu}\left(\frac{\partial E_y}{\partial z} - \frac{\partial E_z}{\partial y}\right)$$

$$\frac{\partial H_z}{\partial t} = \frac{1}{\mu}\left(\frac{\partial E_z}{\partial x} - \frac{\partial E_x}{\partial z}\right)$$

$$\frac{\partial E_x}{\partial t} = \frac{1}{\varepsilon}\left(\frac{\partial H_z}{\partial y} - \frac{\partial H_y}{\partial z}\right)$$

$$\frac{\partial E_y}{\partial t} = \frac{1}{\varepsilon}\left(\frac{\partial H_x}{\partial z} - \frac{\partial H_z}{\partial x}\right)$$

$$\frac{\partial E_z}{\partial t} = \frac{1}{\varepsilon}\left(\frac{\partial H_y}{\partial x} - \frac{\partial H_x}{\partial y}\right)$$

And then we can get:

$$H^{n+\frac{1}{2}} = H^{n-\frac{1}{2}} + \frac{\Delta t}{\mu}\nabla \times E^n$$

The difference in space domain then becomes:

$$\frac{\partial F^n(i,j,k)}{\partial x} = \frac{F^n(i+1/2,j,k) - F^n(i-1/2,j,k)}{\Delta x}$$

$$\frac{\partial F^n(i,j,k)}{\partial y} = \frac{F^n(i+1/2,j,k) - F^n(i-1/2,j,k)}{\Delta y}$$

$$\frac{\partial F^n(i,j,k)}{\partial z} = \frac{F^n(i,j,k+1/2) - F^n(i-1/2,j,k-1/2)}{\Delta z}$$

For example, if we want to derive TM polarization in 2D, we calculate the differential

equation $\nabla \times H^{n-\frac{1}{2}}$ and then substitute in the differential formula:

$$E_z^n(i,j) = \frac{1 - \dfrac{\sigma(i,j)\Delta t}{2\varepsilon(i,j)}}{1 - \dfrac{\sigma(i,j)}{2\varepsilon(i,j)}} \bullet E_z^{n-1} +$$

$$\frac{\dfrac{\Delta t}{\varepsilon(i,j)}}{1 + \dfrac{\sigma(i,j)\Delta t}{2\varepsilon(i,j)}\Delta x}\left\{H_y^{n-\frac{1}{2}}\left(i+\frac{1}{2},j\right) - H_y^{n-\frac{1}{2}}\left(i-\frac{1}{2},j\right)\right\} -$$

$$\frac{\dfrac{\Delta t}{\varepsilon(i,j)}}{1 + \dfrac{\sigma(i,j)\Delta t}{2\varepsilon(i,j)}\Delta y}\left\{H_x^{n-\frac{1}{2}}\left(i,j+\frac{1}{2}\right) - H_y^{n-\frac{1}{2}}\left(i+\frac{1}{2},j\right)\right\}$$

$$H_x^{n+\frac{1}{2}}\left(i,j+\frac{1}{2}\right) = H_x^{n-\frac{1}{2}}\left(i,j+\frac{1}{2}\right) - \frac{\Delta t}{\mu\left(i,j+\frac{1}{2}\right)}\frac{1}{\Delta y}\left\{E_z^n(i,j+1) - E_z^n(i,j)\right\}$$

$$H_y^{n+\frac{1}{2}}\left(i+\frac{1}{2},j\right) = H_y^{n-\frac{1}{2}}\left(i+\frac{1}{2},j\right) - \frac{\Delta t}{\mu\left(i+\frac{1}{2},j\right)}\frac{1}{\Delta x}\left\{E_z^n(i+1,j) - E_z^n(i,j)\right\}$$

Of course, we can obtain TE polarization in 3D by similar procedure.
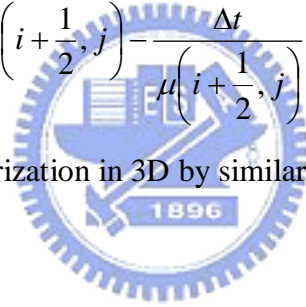
2.3 The Basic Simulation of Microdisk and Microgear

In our FDTD simulations, at first, we assume a circular-shaped microdisk composed by dielectric disk surrounded by air shown in Fig. 2.1 (a) with disk size of 0.9 μm in diameter and effective index of 2.73, which are aimed at sustaining $WG_{6,1}$ mode at 1.5 to 1.6 μm and correspond to modal index of TE-polarized fundamental mode in InGaAsP MQWs slab with thickness of 220 nm. The typical simulated $WG_{8,1}$ mode in microdisk in magnetic field is shown in Fig. 2.1 (b).

At first, we would like to find out the relation between the azimuthal number of WG mode and their Q factors. Form the simulated result in Fig. 2.2 and Table I, we can observe

the Q factor increases exponentially and the wavelength decreases linearly when the azimuthal number of WG mode increases. From the physical meanings, when the azimuthal number increases, more lobes will be talent in the microdisk with the same radius and this will lead to the wavelength increasing. At the same time, when azimuthal number increases under the invariant disk size, for each lobe of WG mode with higher azimuthal number will be suffered from smaller localized bend loss and then the Q factor will increase exponentially.
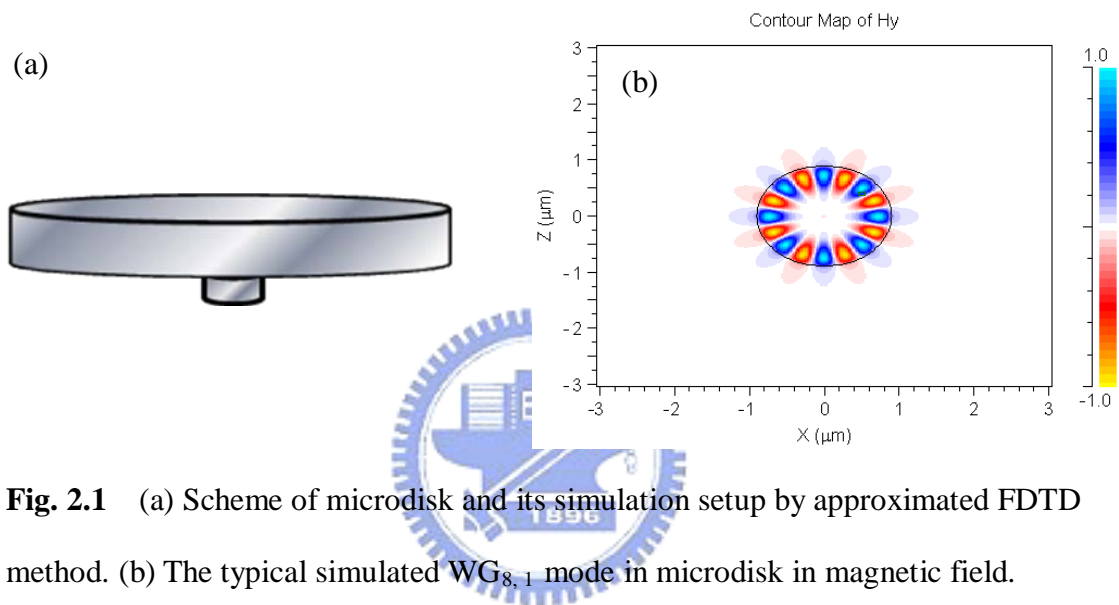
Fig. 2.1   (a) Scheme of microdisk and its simulation setup by approximated FDTD method. (b) The typical simulated $WG_{8,1}$ mode in microdisk in magnetic field.
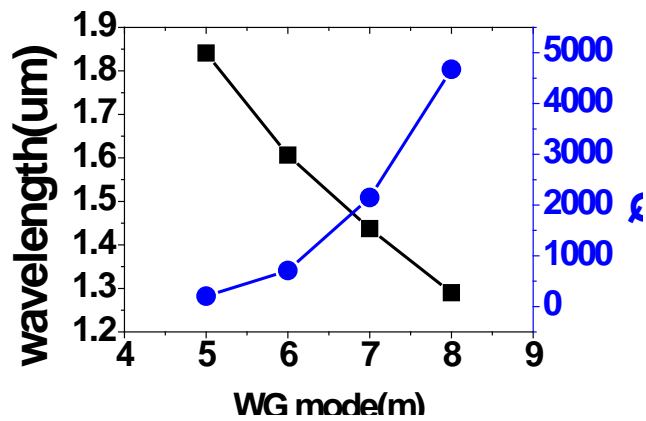
Fig. 2.2   The relationship between simulated wavelength and Q factor of WG mode with different azimuthal numbers from 5 to 8.

Table I The simulated wavelength and Q factor of WG mode with different azimuthal numbers.

WG Mode	Wavelength (μm)	Q Factor
5	1.8409	203
6	**1.6063**	**709**
7	1.4372	2147
8	1.2901	4673

And then we further considerate the effect of changing microdisk size on Q factor. The microdisk radius (R) is changed from 500 to 900 nm. According to the researches in next chapter, the target mode is chosen as $WG_{6,\,1}$ mode. The simulated relation of radius, wavelength and Q factor are shown in Fig. 2.3 and Table II. We can observe the wavelength increases with the microdisk radius, which is caused by the same reason we discussed in last paragraph. But we also find out that the Q factor does not change significantly when the disk size increases. The possible reason is that the change of radius is not large enough to affect the Q factor variation.
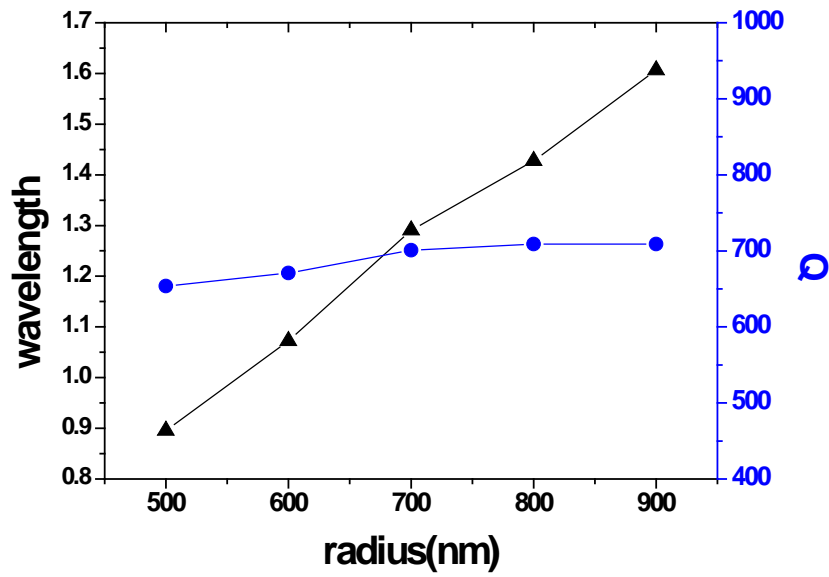
Fig. 2.3 The relationship of wavelength, Q factor and radius

**Table II** The relationship of wavelength, Q factor and radius

R	wavelength	Q
500	0.8953	653.5
600	1.0726	670.9
700	1.299687	701
800	1.4278	709.2
900	**1.60627**	**709**

And then we transform the microdisk we optimized above to be micro-gear by adding the periodic gratings with grating width (W) from 0.15 to 0.325 μm, grating height (H) from 0.025 to 0.175 μm, and the micro-gear radius is fixed as 0.9 μm, as defined in Fig. 2.4. The

calculated Q mapping is shown in Fig. 2.5 (a) and Table II. The high Q factor of 1,190 is obtained when $W = 0.175$ μm and $H = 0.125$ μm, which is 73 % enhanced compare with that of original microdisk. And the simulated mode profile in magnetic field is shown in Fig. 2.5 (b).
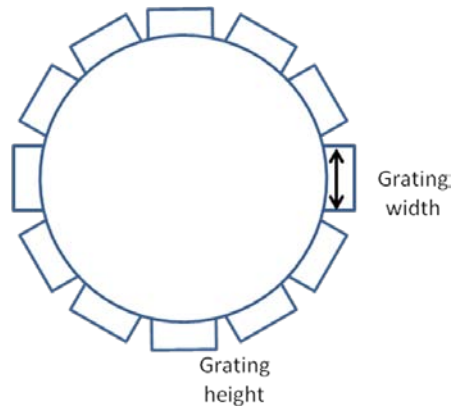
**Fig. 2.4**   The scheme of micro-gear and the definition of grating width and height.
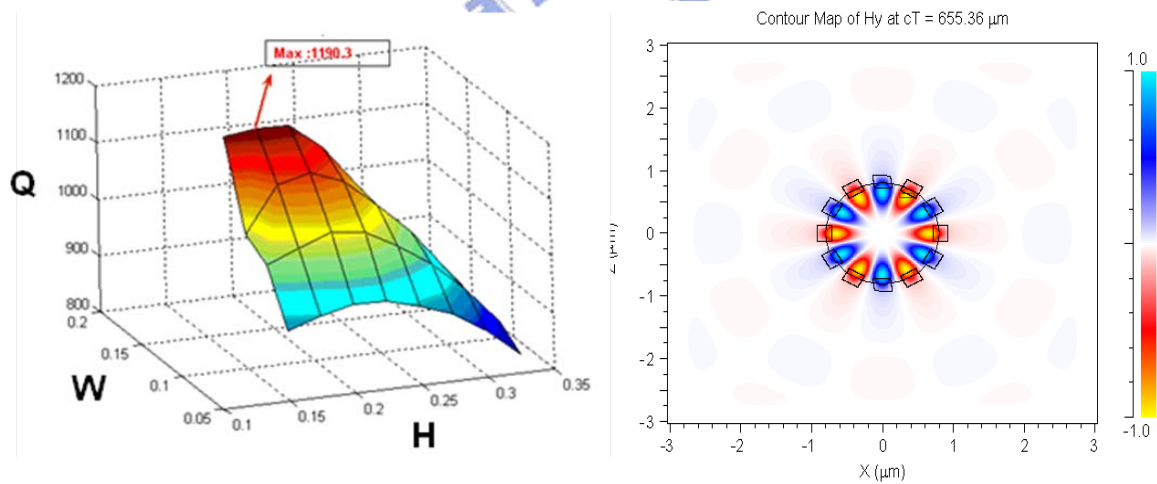
Fig. 2.5   (a) The simulated Q factor mapping of grating height (H) and grating width (W) from $WG_{6,1}$ mode. (b) The simulated $WG_{6,1}$ mode profile in magnetic field when $H = 0.125$ μm and $W = 0.175$ μm.

Table III The simulated Q factor from $WG_{6,1}$ mode in microgear with different grating height (H) and width (W).

W(μm) H(μm)	0.05	0.075	0.1	0.125
0.15	924.7	1012.2	1037.5	1182.4
0.175	942.23	1035.4	1118.2	**1190.3**
0.2	956.6	1055.3	1132.3	1187.4
0.225	955.72	1048.3	1110.4	1141.94
0.25	938.3	1016.6	1061.8	1068.3
0.275	919.3	977.81	1008	999.1
0.3	880.9	925.5	936.3	925.0
0.325	833.4	862.5	865.9	851.6

From Fig. 2.5 (a) and Table III, we can find that the Q factor of WG6, 1 mode is much sensitive in H variation than in W variation under the similar variation units. Approximately, under the fixed W, the Q factor increases when H increases. This can be attributed to the reduced bend loss due to the elongated circumference length caused by increased H.

Besides, we also wonder the WG modes with other azimuthal number when micro-gear with M = 6. The microgear parameters are set to be the optimized H and W. The simulated Q factors are shown in Fig. 14 (a). As one can see from Fig. 14 (a), except for the $WG_{6,1}$ mode we optimized, the Q factors of other WG mode will be greatly suppressed compared with those in original microdisk. That means the micro-gear will be induce extra loss and destroy those WG modes with azimuthal numbers mismatch with the micro-gear. The simulated WG mode spectra of microdisk and micro-gear with M = 6 shown in Fig. 2.6 (b) also clearly indicates this fact. This side mode suppression approach is important and useful in microdisk semiconductor lasers for single mode lasing.
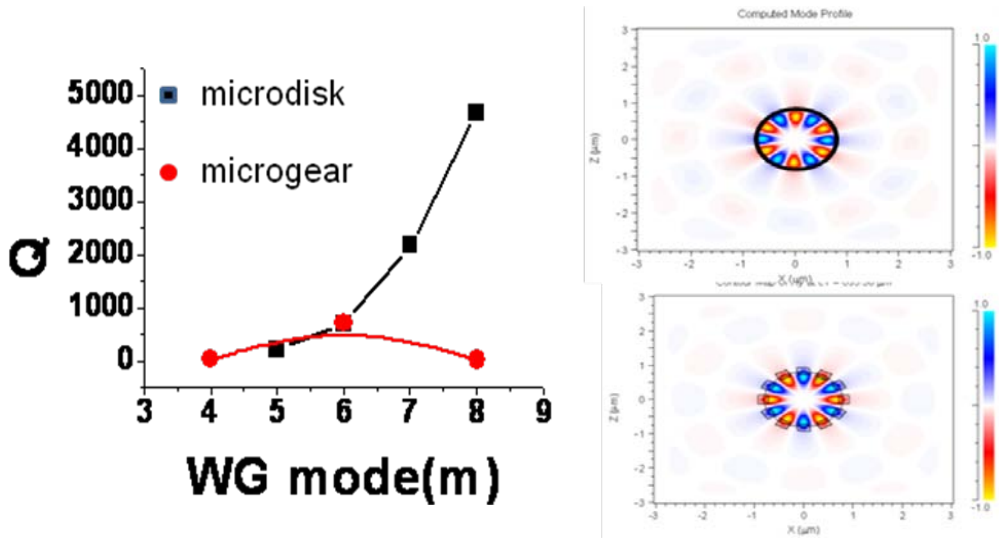
Fig. 2.6 The simulated Q factor from $WG_{6,1}$ mode in microgear with different grating height (H) and width (W).(a) The simulated Q factor of WG mode with azimuthal number 4 to 10 in micro-gear with M = 6. (b) The simulated WG mode spectra of microdisk (Top) and micro-gear with M = 6 (bottom).
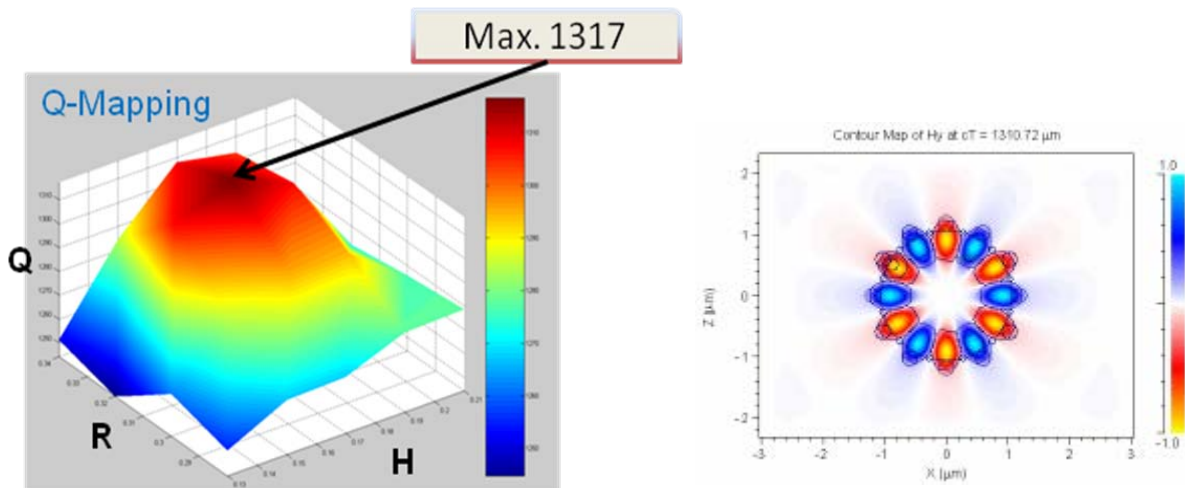
2.4 Microflower

Instinctively, to further reduce the bend loss locally, the grating boundary in micro-gear should become "smoother". In other words, the boundary should be more fit with the $WG_{6,1}$ mode profile. Thus, based on the optimized parameters in micro-gear in last paragraph, we further tune the grating profile by parameter of radius (R) and transform it to be so-called "micro-flower". The scheme and parameter definition are shown in Fig. 2.7. We can observe that the microflowers are designed by modifying the gears of microgear from rectangle to curve. Besides, due to the high sensitivity of H on Q factor we simulate before, we also fine tune the H parameter in the optimization.

We calculate the $WG_{6,1}$ mode Q factor mapping under $R = 0.4$ to 0.45 μm and $H = 0.1$ to 0.2 μm, with fixed $W \sim 0.175$ μm. From the calculated Q mapping shown in Fig. 2.8 (a) and Table IV, we obtain the highest Q factor of 1,317 when $R = 0.32$ μm and $H = 0.17$μm, which is 94 % and 23 % enhanced compared with that in original microdisk and micro-gear. The simulated $WG_{6,1}$ mode profile is also shown in Fig. 2.8 (b). Although the Q factor enhancement is not as large as that from microdisk to micro-gear, this small enhancement is still agree with our assumption before.
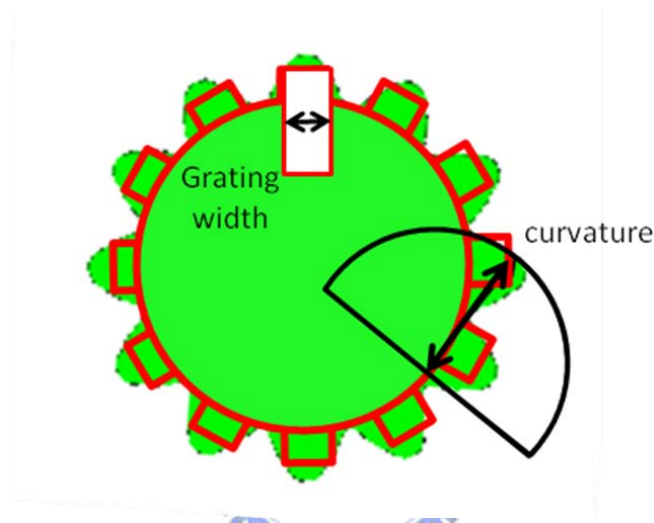
Fig. 2.7 The scheme and the parameter R definition of micro-flower.

Fig. 2.8 (a) The simulated $WG_{6,1}$ Q factor mapping in micro-flower with different height (H) and curvature (R). (b) The simulated $WG_{6,1}$ mode profile in magnetic field in micro-flower.

Table IV The simulated WG$_{6,1}$ Q factor with different micro-flower height (H) and curvature (R)

H \ R	0.28 μm	0.3 μm	0.32 μm	0.34 μm
0.13 μm	1254.8	1261.9	1244.2	1251.2
0.15 μm	1267.1	1285.3	1307.8	1284.5
0.17 μm	1267.9	1295.6	1317.3	1308.0
0.19 μm	1277.7	1294.2	1307.5	1303.3
0.21 μm	1278.5	1276.0	1272.3	1276.0

2.5　Conclusion

In this chapter, we have investigates and discussed the basic WG modal properties in microdisk by approximated FDTD simulations, including the loss mechanism and the Q factor optimization. By using micro-gear topology, we optimize the Q factor by tuning the grating height and width and obtain $Q \sim 1,276$ from WG$_{6,1}$ mode, which is 94% enhancement compared with that in original microdisks. We also observe the mode suppression effect of those WG mode mismatch with the micro-gear. Finally, we further optimize the micro-gear to be micro-flower topology by modifying the grating boundary to be smooth. And high Q of 1,317 is obtained from WG$_{6,1}$ mode.

# Chapter 3 Photonic Crystal Circular-Shaped D_2 (CD$_2$) Microcavity

3.1 Introduction and Motivation

From the last two chapters, we also know the performance is worse when the microdisk is in small volume. In last chapter, we have confirmed that the confinement will be getting better and the Q factor will be increased when the cavity boundary of microdisk is more fitting with the WG mode. However, from our previous simulations, we know that the Q factor is also difficult to get a huge breakthrough even we modify the boundary of microdisk by micro-gear or micro-flower topologies when the microcavity size comes close to wavelength scale. To overcome this bottleneck, we apply and design a new photonic crystal microcavity and study on the enhanced WG mode in it. In addition, according to the similar approach in optimizing microdisk, we also investigate and verify whether we can get ultra-high Q factor by modifying the cavity boundary of photonic crystal microcavity or not.

In this chapter, at first, we will introduce the fabrication process of photonic crystal microcavity. And then, we will introduce the design concept of photonic crystal CD$_2$ microcavity. We will also introduce the result of simulation and design the photonic crystal CD$_2$ with micro-flower topology. And then, we will introduce the process of micro-flower and the measurement results. Finally, there will be a brief conclusion

.

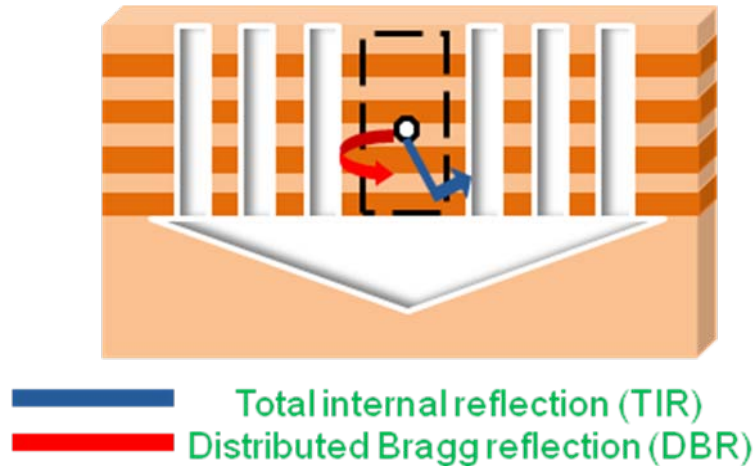## 3.2 Fabrication of Photonic Crystal Membrane Microcavity

The structure of photonic crystal are shown in Fig. 3.1, the epitaxial structure consists of four 1.2 % compressively strained InGaAsP multi-quantum-wells (MQWs), which are separated by 20 nm unstrained InGaAsP barriers. The measured PL spectrum with bandwidth from 1420 to 1580 nm and centered at 1550 nm in the active epitaxial layer is obtained.
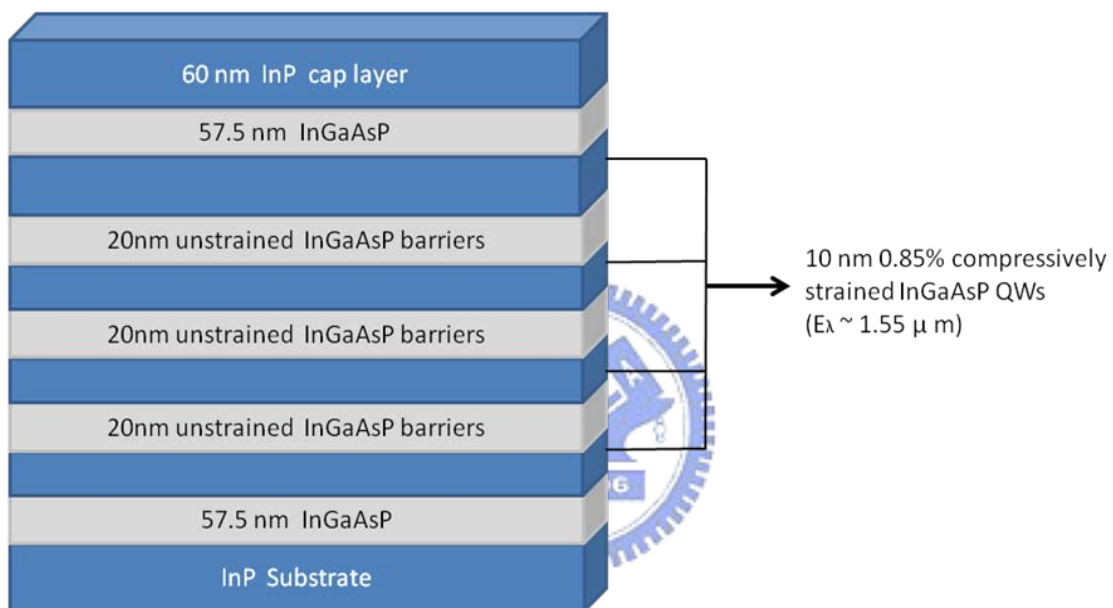
Fig. 3.1 The epitaxial structure for membrane photonic crystal microcavity.

The scheme of photonic crystal membrane microcavity is shown in Fig. 3.2. In this kind of microcavity, the PBG effect is used for optical confinement as perfect mirrors in the in-plane direction and the TIR at the interface between the slab and the air cladding mainly provides the optical confinement in the vertical direction.
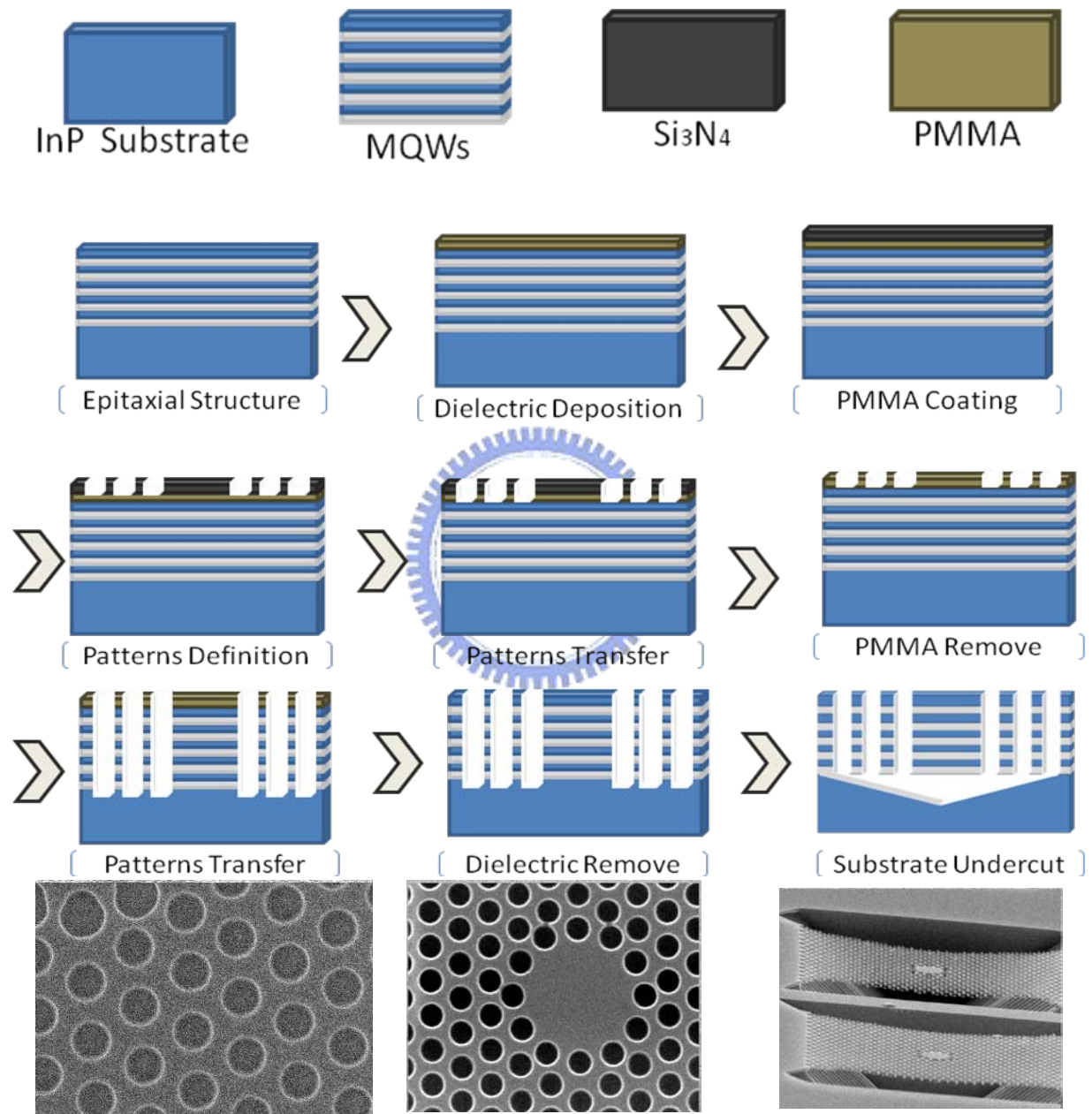
Fig. 3.2 The scheme of photonic crystal membrane microcavity structure.

At first step of the process, the Si₃N₄ layer with 140 nm on the wafer as an etching hard mask is deposited. The thickness of Si_3N_4 is decided by the selective dry etching ratio in the following pattern transferring process. And then we use the spin-coater to spin-coat an A5 polymethylmethacrylate (PMMA) resist layer on the surface by two spinning steps, 1,000 rpm for 10 seconds and 3,500 rpm for 25 seconds. The photonic crystal patterns are defined on PMMA by using electron-beam lithography EX-7500. Finally, the pattern will be in a series developing and fixing

.

In order to transfer the patterns into the following layers, the Oxford Plasma-Lab-100 inductively coupled plasma / reactive ion etching (ICP/RIE) system is used. The pattern will be transferred into the Si_3N_4 hard mask by CHF_3/O_2 mixed gases in RIE mode dry etching. And then the pattern will be further transferred into the InGaAsP MQWs by $H_2/CH_4/Cl_2$ mixed gases in ICP mode dry etching process.

Finally, the InP substrate below the MQWs will be removed and the undercut can be constructed by selective wet-etching with mixture solution of HCl : H_2O= 3 : 1 at 2 ℃ for 8

minutes. The fabrication process overview of 2D photonic crystal membrane structure is shown in Fig. 3.3. The tilted- and top-view SEM picture of fabricated devices are also shown in Fig. 3.3

.

Fig. 3.3   The fabrication process overview of 2D photonic crystal membrane

microcavity. The tilted- and top-view SEM pictures are also shown.

3.3   The Basic Design and Simulation of Photonic Crystal CD2

In recent years, although the micro and nanocavities formed by photonic crystal with PBG effect have successfully overcome above performance degradations and show excellent performances including high Q-factor and low threshold when minimizing the cavity size, in most present commonly-used photonic crystal cavity designs, WG mode is rarely well-sustained or not the only mode able to laze in the designed range. In our previous report [21], we have shown a strong WG mode dependence on the boundary geometry of 12-fold QPC microcavity (positions of 12 nearest air holes) and this will provide us a design direction to enhance WG mode in photonic crystal microcavity.

In micro-disk lasers we investigate in chapter 2, it has been proof that we can enhance specific WG mode by shaping the microcavity, for example, micro-gear and micro-flower topologies. And the specific WGM with azimuthal lobes that match with the gears will be well sustained and other resonance modes including ∂-phase shifting mode, WG modes with mismatched azimuthal lobes, and different order WG modes will be weaken. Recently, we have reported that the gears formed by 12 nearest air holes in 12-fold QPC microcavity also show the similar effect as in micro-gear lasers. And we have demonstrated this idea in experiments with high Q-factor of 10,000, low threshold of 0.15 mW, and strong WG mode dependence on the cavity geometry due to this micro-gear effect. As a result, it is possible to sustain a WG in photonic crystal D_2 microcavity by shifting the 12 nearest air holes slightly.

The scheme of our design is shown in Fig. 20. The PCs are formed by air holes on a thin dielectric slab and the original photonic crystal D_2 microcavity is formed by removing seven air holes. The positions of 12 nearest air holes are rearranged to form circular boundary geometry with spacing of one lattice constant by moving six of them inward and six of them

outward, which is re-named photonic crystal circular-D_2 (CD_2) microcavity due to its cavity

shape, as shown in Fig. 3.4.
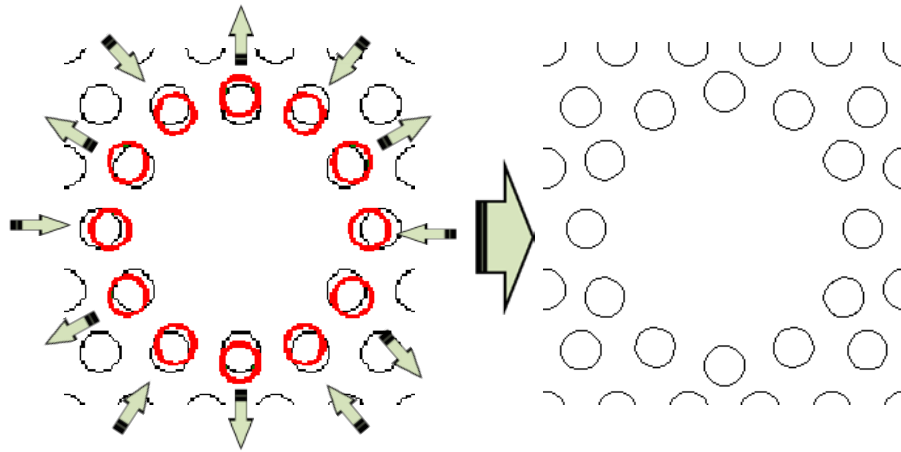
Fig. 3.4   The scheme and cavity design of photonic crystal CD_2 microcavity.

To confirm this design, we apply three-dimensional 3D FDTD method to simulate the

WG modal characteristics in photonic crystal CD_2 microcavity. The designed lattice constant

(*a*) and the air-hole radius (*r*) over lattice constant ratio (*r/a*) are 500 nm and 0.34. The

refractive index of the dielectric material (InGaAsP) is set as 3.4. The simulated electrical

field distributions in the *x-z* and *x-y* plane of sustained $WG_{6,1}$ mode with azimuthal number

six whose lobes match with the gears formed by the 12 nearest air holes are shown in Fig. 3.5.

From the mode distribution in the *x-z* plane, one can observe a significant zero-distribution

region at the center of the microcavity. This indicates that this mode can be considered a good

candidate of excited mode for the electrical injection structure by inserting a central post

without affecting WG mode lasing performance.
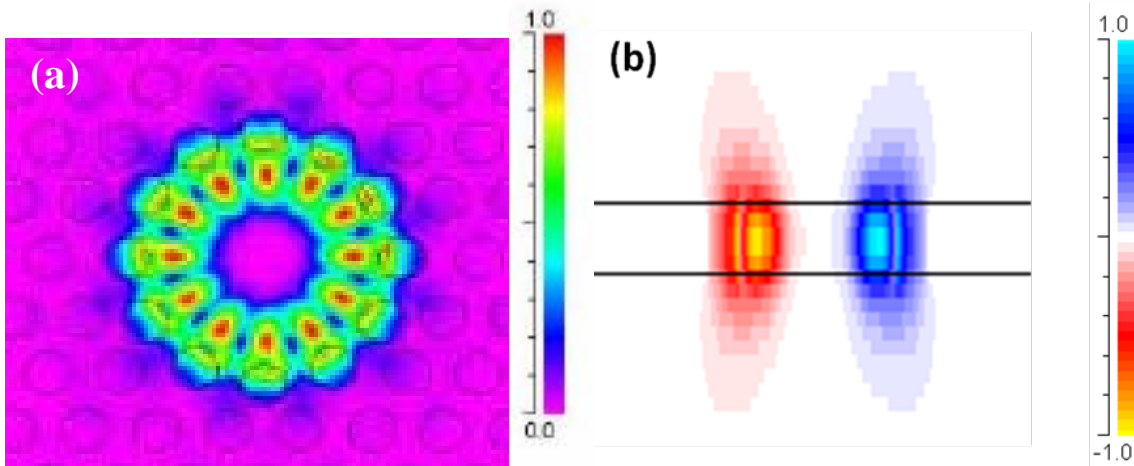
Fig. 3.5 The simulated WG$_{6,1}$ mode profile in electrical field in the (a) *x-z* plane and (b) *x-y* plane.

In the Fig. 3.5 (b), it is also observed from the electric field in the *x-y* plane that only a very small fraction of energy radiates into vertical directions due to the modal cancellation of WG mode, which implies its high *Q*-factor. We also calculate and obtain the other WG mode, including WG$_{3,2}$, WG$_{4,1}$, WG$_{5,1}$, and WG$_{7,1}$.

3.4 Microflower Topology on Photonic Crystal CD$_2$ Microcavity

3.4.1 FDTD Simulation

Then we will try to apply the concept of micro-flower topology on the photonic crystal CD$_2$ microcavity with WG$_{6,1}$ mode. In micro-flower, we have modified the boundary to match WG$_{6,1}$ mode in chapter 2. As results, we can initially use the same condition on the boundary of photonic crystal CD$_2$ to match WG$_{6,1}$ mode. And then we will further optimize it. Being similar with the micro-flower topology in micro-disk, we realize the micro-flower

topology by modifying the boundary of CD_2 microcavity by changing the nearest air-hole shape to be partial-curved circle as shown in Fig. 3.6 (a).
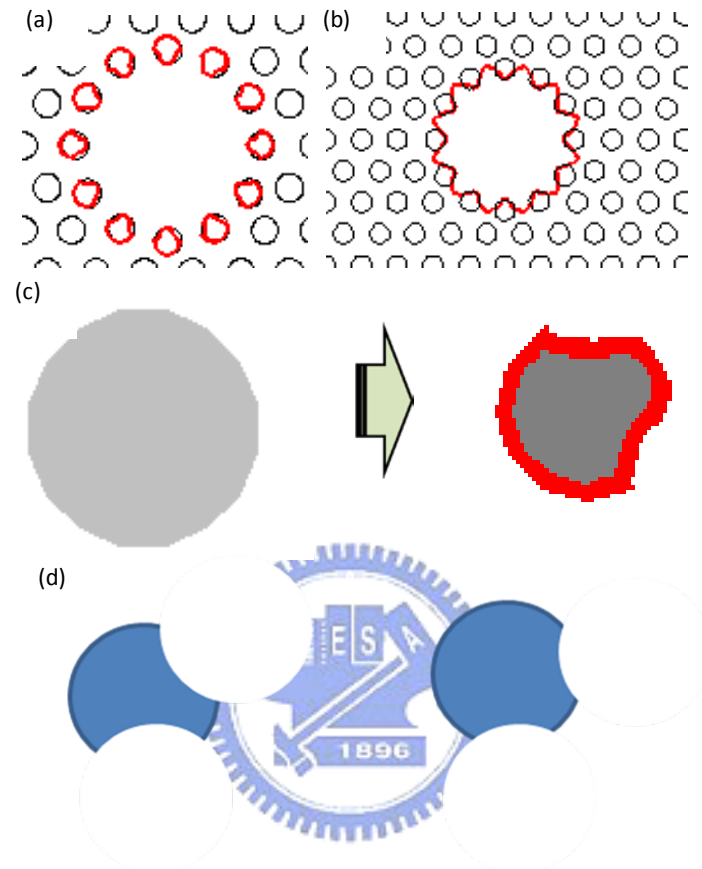
Fig. 3.6 (a)-(d) The scheme of applying micro-flower topology on photonic crystal CD_2 microcavity.

At this time, we let the microflower fit the nearest air holes of photonic crystal CD_2 microcavity, as shown in Fig. 3.6 (b). The change in each air hole is also shown in Fig. 3.6 (c). In the simulations, the lattice constant, *r/a* ratio, and refractive index are set to be 500 nm, 0.32, and 3.4, respectively. Fit different curvature of micro-flower to photonic crystal CD_2 microcavity by the air holes with different curvatures are shown in Fig. 3.6 (d).

By 3D FDTD simulations, the simulated $WG_{6,1}$ mode in electric field in photonic crystal micro-flower CD_2 ($MFCD_2$) microcavity is shown in Fig. 3.7. By varying the air-hole curvature R, the simulated vertical Q factor variation of $WG_{6,1}$ mode are also shown in Fig. 3.8 and Table V.
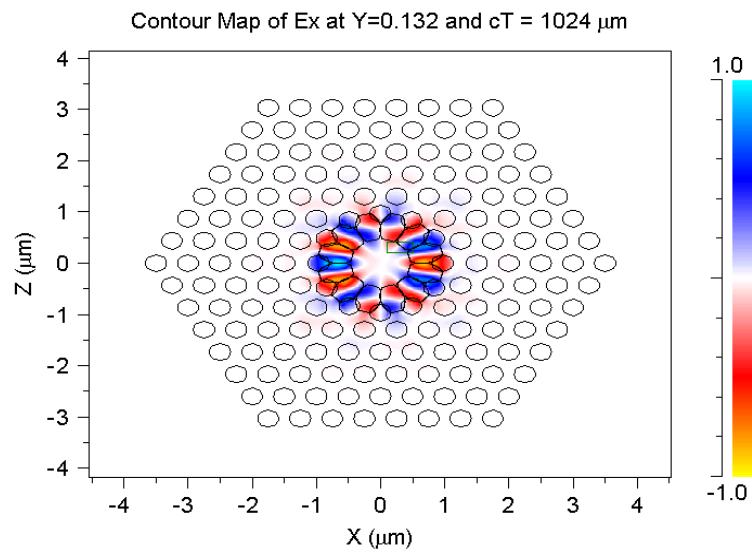
Fig. 3.7   The simulated $WG_{6,1}$ mode profile in electric field in photonic crystal $MFCD_2$ microcavity.
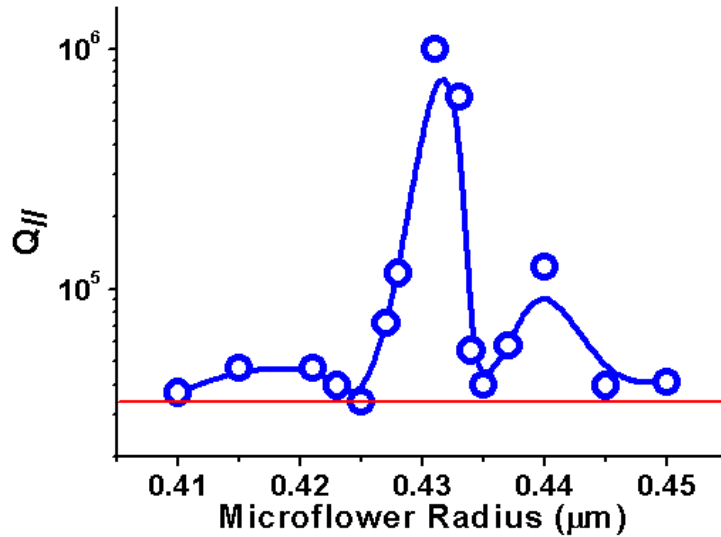
Table V The table of simulated $WG_{6,1}$ vertical Q factor and air-hole curvature R.

Curvature (μm)	Q (vertical)	wavelength(μm)
0.41	36905	1590.354
0.415	46577	1585.257
0.421	46775	1585.257
0.423	39562	1585.257
0.425	33671	1585.257
0.427	72207	1583.958
0.428	116000	1583.787
0.431	999000	1582.842
0.433	633000	1582.842
0.434	55319	1582.842
0.435	39666	1577.719
0.437	57918	1580.192
0.44	123300	1580.192
0.445	39462	1575.46
0.45	41007	1580

Fig. 3.8 The relationship between the simulated $WG_{6,1}$ vertical Q factor and air-hole curvature R.

From Fig. 3.8 and Table V, we found that the curvature is inverse-proportional to the wavelength. The vertical Q factor is enhanced from R = 0.41 - 0.45 um. Furthermore, we obtain large vertical Q enhancement in some specific curvatures, for example, R = 0.425 - 0.435 um. When R = 0.431 um we even obtained enhanced vertical Q factor of 1,000,000, which is over 30-fold enhancement compared with the original vertical Q factor in photonic crystal CD_2 microcavity (horizontal line in Fig. 3.8). This also directly indicates that the micro-flower topology plays the role of vertical loss reducer in photonic crystal CD_2 microcavity

.

3.4.2 Device Fabrication

At first, the photonic crystal CD_2 microcavity pattern is defined by AutoCAD tools, as shown in Fig. 3.9 (a). At the same time we will draw widow regions on both sides of the photonic crystal pattern in order to achieve InP undercut in the final selective wet-etching,

33

as shown in Fig. 3.9 (b). Finally, we will modify the nearest air-hole to be partial-curved shape and form the micro-flower topology, as shown in Fig. 3.9 (c). We should mention that when the holes are defined to be dodecagon, the nearest holes should be dodecagon, so that the pattern would be effectively definition.

The SEM pictures of fabricated result are shown in Fig. 3.10 (a) - (d). We can clearly see the membrane structure after selective wet-etching process in Fig. 3.10 (b), and the micro-flower topology formed by partial-curved air-hole in Fig. 3.10 (d)
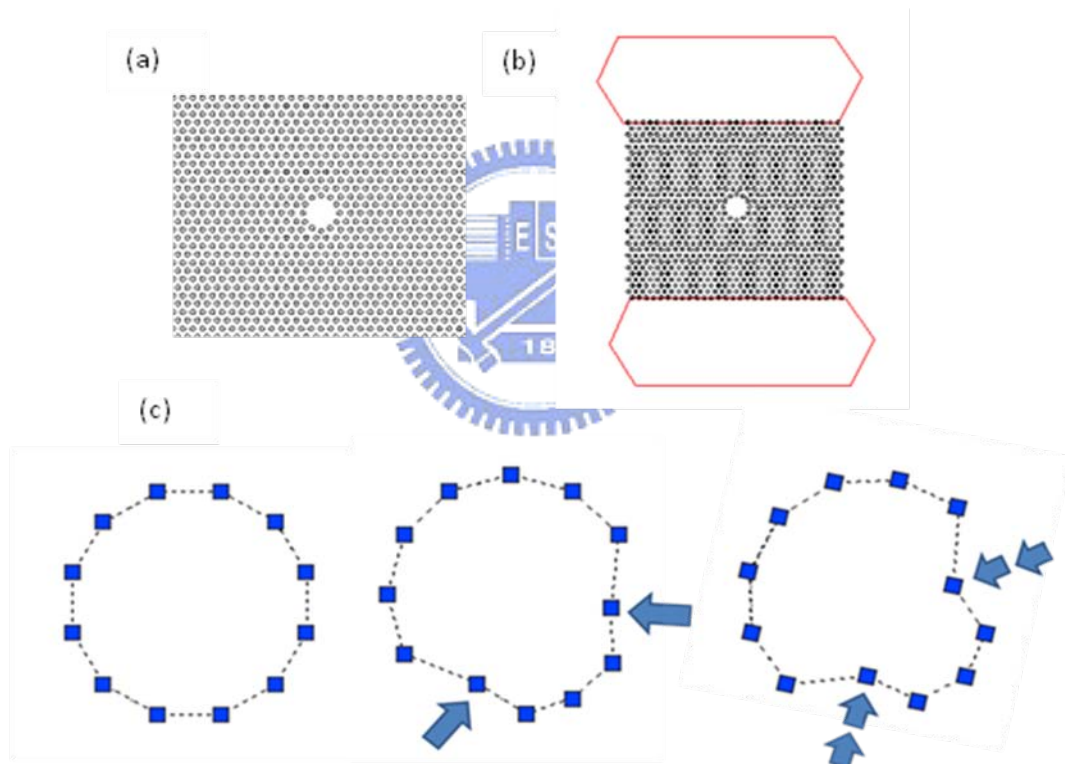
Fig. 3.9   (a)-(c) The definition of photonic crystal MFCD$_2$ microcavity by AutoCAD tools.
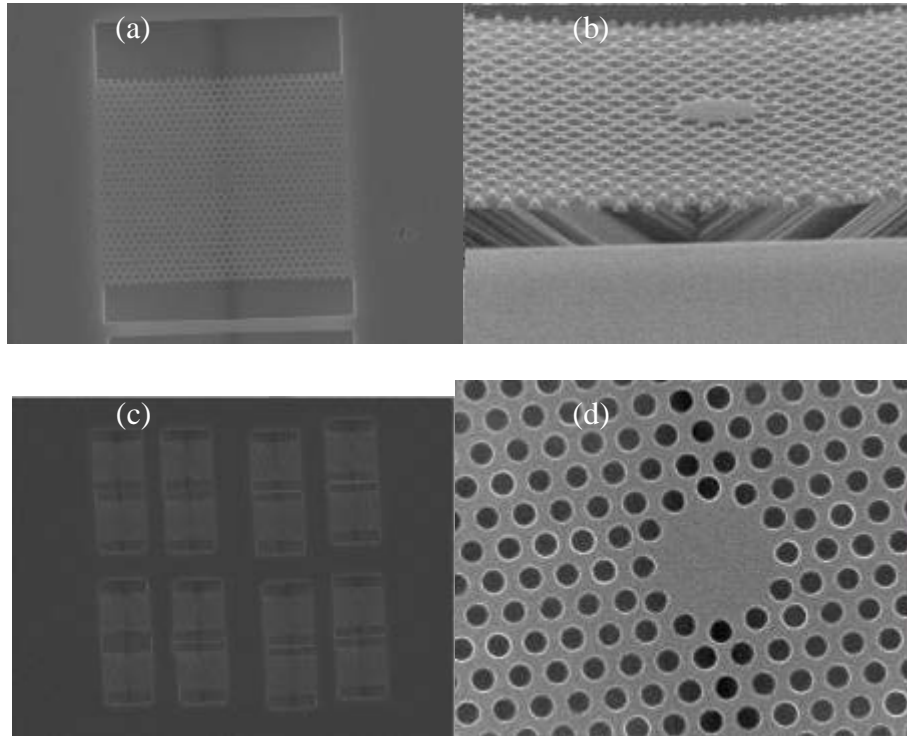
Fig. 3.10 The (a) top-, (b) side-, and (c) over-view SEM pictures of fabricated photonic crystal $MFCD_2$ microcavity. (d) The micro-flower topology formed by nearest partial-curved air-hole shape.
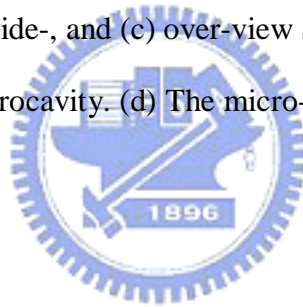
3.5 Measurements

3.5.1 Measurement System Setup

We use a micro-photoluminescence (micro-PL) system with sub-micrometer scale resolution in space and sub nanometer scale resolution in spectrum in order to measure the lasing characteristics of our fabrication device. The simple configuration of the micro-PL system is shown in Fig. 3.11.

The objective lens collects the emitted light from the top of the sample. We use a collective lens to focus the output signal into the slit of our optical spectrum analyzer, with

0.05nm resolution. An InGaAs detector with good responsibility from 900nm to 1600nm is used to obtain the lasing spectra of our devices. All of the following measurement results are measured by this micro-PL system.
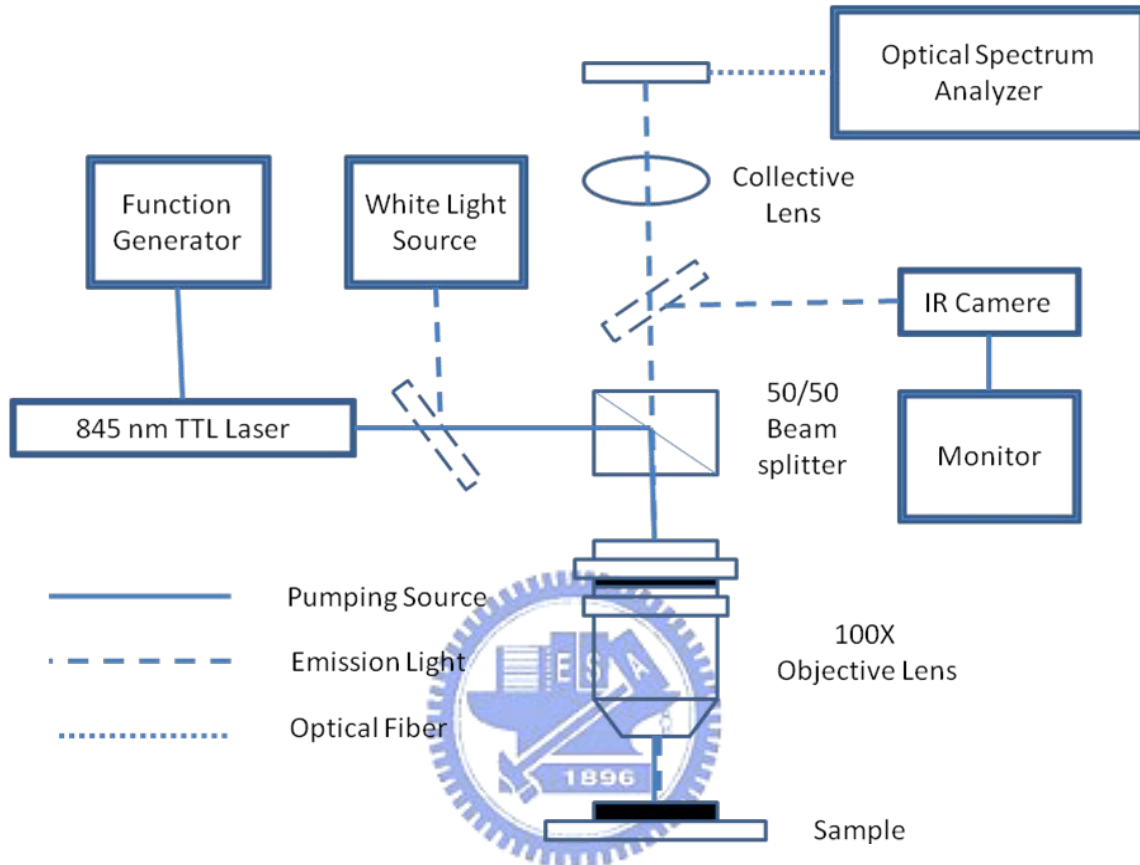
Fig. 3.11 The configuration of NIR micro-PL system setup.

3.5.2 The Lasing Characteristic of WG Mode in Microflower

To investigate WG mode in photonic crystal CD_2 microcavity, in FDTD simulations, we vary the lattice constant and find out the normalize frequency of microflower match that of photonic crystal CD_2 microcavity. The relationship between normalize frequency of $WG_{6,1}$ mode and lattice constant is shown in Fig. 3.12 (a). The normalize frequencies correspond to the wavelength range from 1430 to 1580 nm. We can still find out a little inaccuracy in Fig. 3.12 (a) because of different fabrication instruments. In Fig. 3.12 (b), we can easily find out the measured lasing peak at 1465.4 nm where $a = 490$ nm.

(a)   (b)
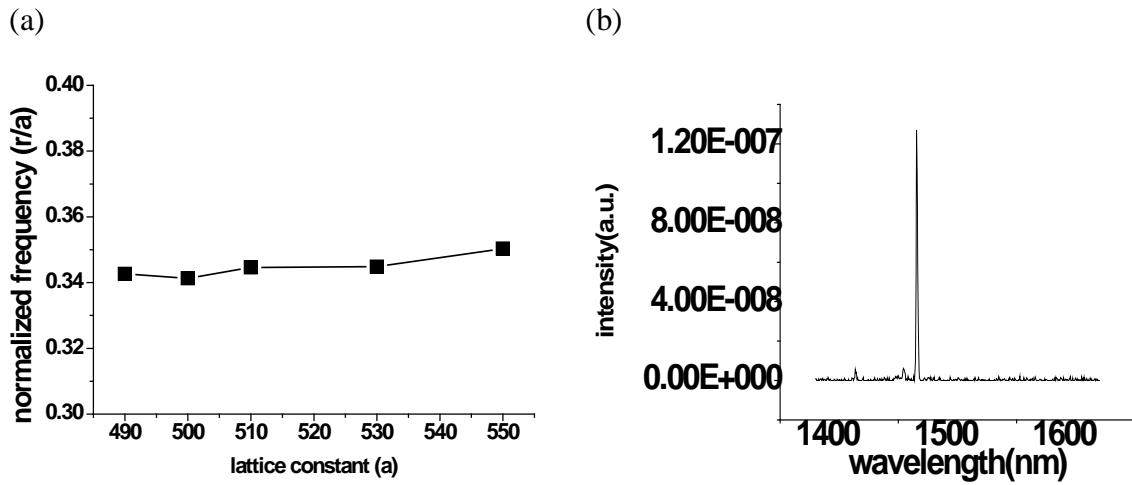
Fig. 3.12 (a) The relationship between normalize frequency and lattice constant. (b) The lasing spectrum at 1465.4 nm of photonic crystal CD_2 microcavity when $a = 490$ nm.

Then, we would like to compare the simulation and measurement result to confirm that weather the confinement performance would be better in photonic crystal $MFCD_2$ microcavity. We investigate Q factor by half-wavelength width by the simple formula of $Q = \lambda / \triangle \lambda$, where λ is the wavelength of WG mode and $\triangle \lambda$ is the line-width of the lasing peak. The measurement results of Q factor and wavelength in photonic crystal $MFCD_2$ microcavity with different curvatures are shown in Fig. 3.13.
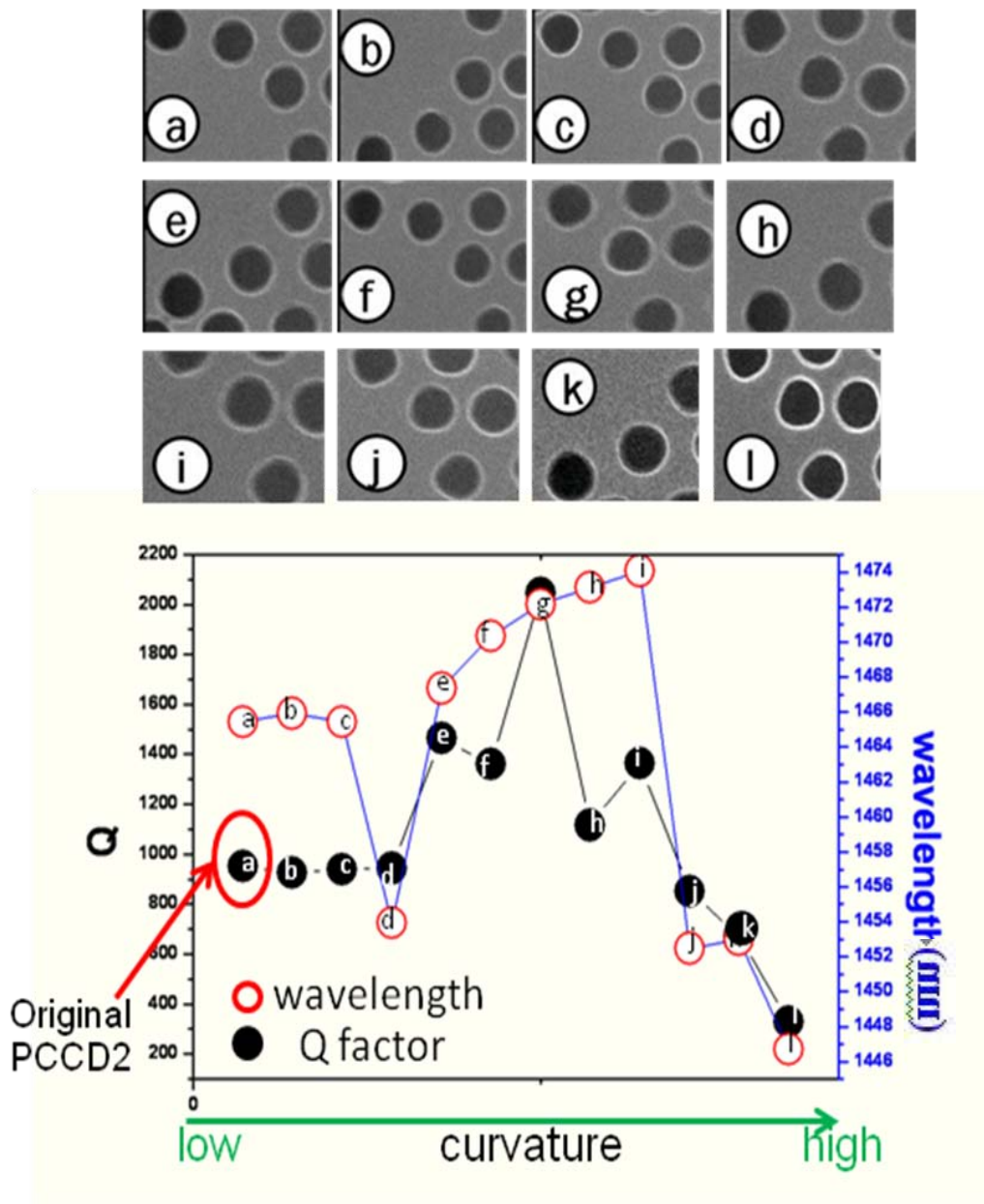
Fig. 3.13 The measurement results of Q factor and wavelength in photonic crystal MFCD$_2$ microcavity with different curvatures.

The SEM picture on the bottom of left in Fig. 3.13 is the photonic crystal CD$_2$ microcavity. From Fig. 3.13, we can observe that at the beginning we modify the holes, the Q factor will not change a lot with the modified air-hole. The Q factor does not change until the air-hole is modified to the right curvature. As getting to the right curvature, the Q factor enhance about 100 % compared with the photonic crystal CD$_2$ microcavity, which confirm

that we can optimize the confinement performance by modifying the air-hole's shape. When the boundary modified to be similar with the WG mode profile, the WG mode would be suffered less vertical optical losses we mention before. The fabrication result is not as good as the simulation result, and that could be probably caused by the fabricated air-hole distortion. Another thing to mention is that when the air-hole's arc becomes larger and larger, the WG mode would be broken and the confinement performance would even worse than the original one.

3.6 Conclusion

In this chapter, we propose a novel photonic crystal microcavity (CD_2 microcavity) design sustaining high Q $WG_{6,1}$ mode by modifying the cavity boundary. The WG modal properties are simulated by 3D FDTD simulations. High Q factor of 38,000 is obtained. And then we apply the optimized micro-flower topology in chapter 2 on the photonic crystal CD_2 microcavity in order to increase the vertical Q factor of $WG_{6,1}$ mode. By further optimizing the curvature of micro-flower topology, we obtain the enhanced vertical Q factor of 1,000,000 from $WG_{6,1}$ mode, which is 30-fold enhancement of original Q factor of $WG_{6,1}$ mode. According to our design, we also fabricated the photonic crystal CD_2 microcavity with micro-flower topology with different curvatures. From the measurement results, we obtain a Q factor variation from different fabricated CD_2 microcavity with micro-flower topology with different curvatures, which agree with our simulated results.

Chapter 4 Double-Layer Photonic Molecules Composed by Photonic Crystal Microcavities

4.1 Introduction

In this chapter, at first, we will introduce the photonic molecule (PM) composed by micro-structures and photonic crystal microcavities, including their applications and bottlenecks. Based on photonic crystal CD_2 microcavity we proposed in last chapter, we will propose a brand new vertical coupled PM based on double layer structure. By using 3D FDTD simulations, basic PM states will be addressed and the tunable PM state properties will be also investigated. Finally, we will also introduce the development of its fabrication process on GaAs based material.
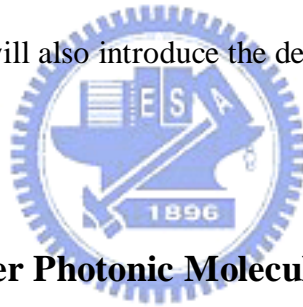
4.2 Design of Double-Layer Photonic Molecule

4.2.1 Design Background & Motivation

PMs have been long regarded as good candidates for components with logical functions in photonic integrated circuits (PICs) due to their special light-matter interactions, which can be analog to electronic states in chemical molecules and achieved by microspheres [22], micro-cylinders [23,24], micro-disks [25-27], and so on, as shown in Fig. 4.1. The simplest and most widely-investigated PM is consisted of two identical semiconductor micro-disks sustaining high Q WG modes, which exhibits unique behaviors including filtering, switching, bistability [26,27], and so on. However, when the size of the micro-disk shrinks due to the

requirement of condensed PICs, serious bend losses caused by small disk radius will lead to degraded performance and limit its application tolerance. In recent years, various micro and nanocavities formed by photonic crystal with PBG effect have overcome this bottleneck [28-31]. By using photonic crystal with PBG effect, several PMs and coupling cavities have also been proposed and reported [32,33] shown in Fig. 4.2, which the photonic crystal cavities are all designed and fabricated on the single membrane, in other words, on the same plane, the same way of designing PMs composed by micro-disks.
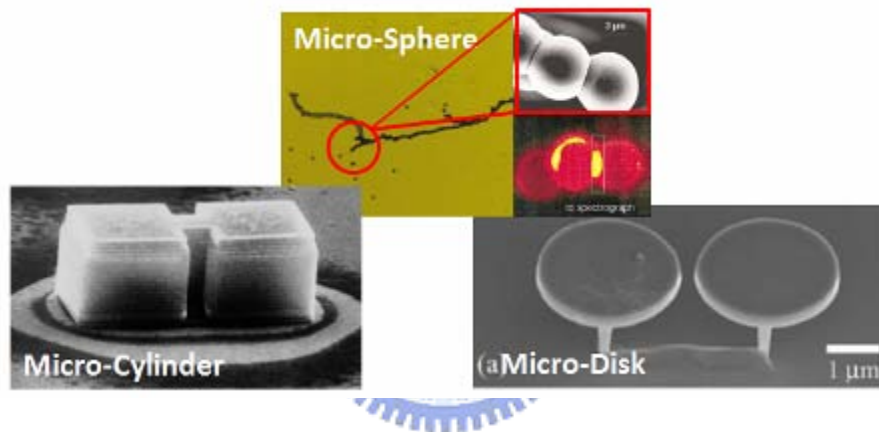
Fig. 4.1 Various PMs composed by microspheres, micro-cylinders, and micro-disks.
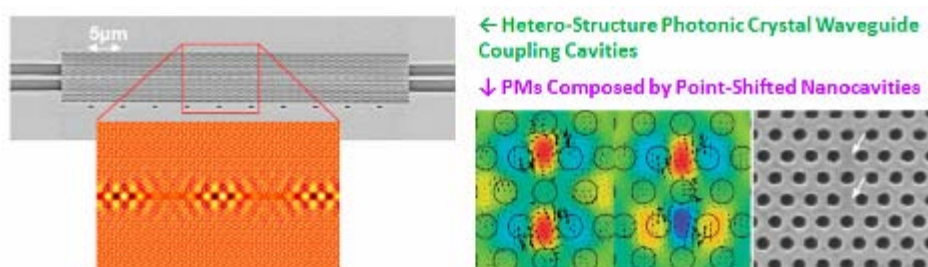

Fig. 4.2 Various PMs composed by photonic crystal microcavity single membrane.

However, there are two main disadvantages for photonic crystal PMs. First, in photonic crystal membrane microcavity, when the surrounded photonic crystal lattice periods are sufficiently large, the main loss (coupling) is dominated only in the vertical direction governed by TIR effect, which is very different from TIR confinement in all directions in micro-disks. Thus, for PMs constructed on single photonic crystal membrane, before coupling, each cavity will suffer extra losses for individual resonance caused by the neighboring cavities, which means the in-plane PBG confinement will be weakened and the Q factors of PMs will be reduced. Second, the geometry of photonic crystal PM on single layer is strongly limited by photonic crystal lattice structure [34], which will limit the variable and controllable abilities of PMs integrated in PICs. It is no doubt that a tunable PM unit can provide more possibilities and flexibilities in constructing functional PICs. Unfortunately, to our best knowledge, there are very few literatures discussing this issue, even in micro-disk systems.

4.2.2 Design Scheme

To solve the issues mentioned above, in this report, we propose a PM design named double-layer PM (DLPM), which is shown in Fig. 4.3, based on the photonic crystal CD_2 microcavity with $WG_{6,1}$ mode we proposed in chapter 3. The DLPM is composed of two identical photonic crystal membranes with thickness and refractive index of 220 nm and 3.4, which can sustain the TE-polarized single fundamental mode in each membrane. According to this structural design, in next paragraph, we will simulate the modal properties of bonding and anti-bonding states based on $WG_{6,1}$ mode existed in DLPM by 3D FDTD simulations. By varying the gap distance and refractive index between the two membranes using mechanical and electrical approaches, we investigate and discuss the controllable DLPM modal properties.
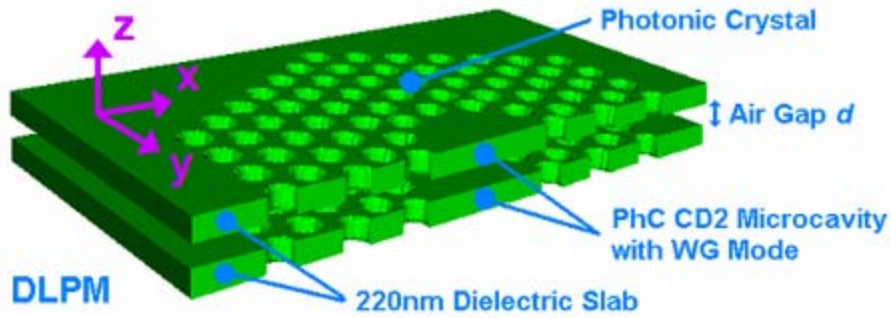
Fig. 4.3 The scheme of DLPM composed by two identical photonic crystal CD_2 microcavity membranes.
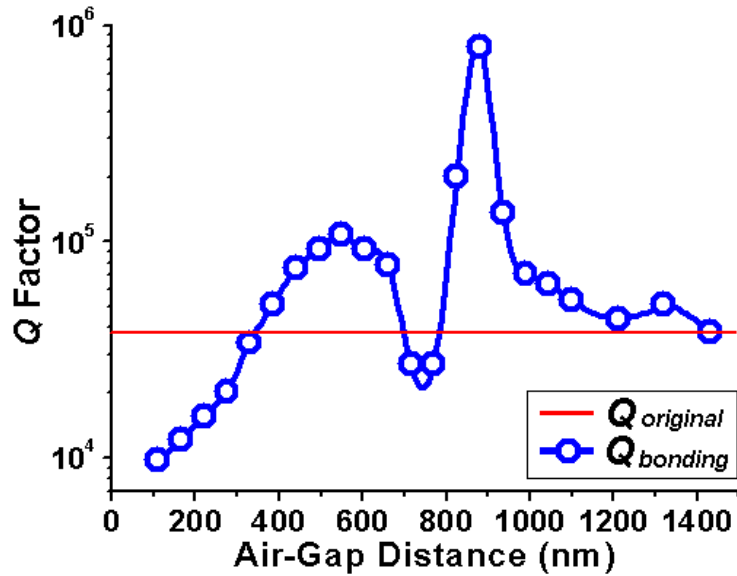
4.2.3 Simulations

The scheme of DLPM composed of two photonic crystal CD_2 microcavity membranes with air-gap distance d in between is shown in 32. In FDTD simulations, the thickness and refractive index of each membrane are set as 220 nm and 3.4 according to the epitaxial structure of InGaAs / GaAs single quantum well with AlGaAs sacrificial layer. The designed lattice constant (a) and air-hole radius (r) over lattice constant ratio (r/a) of photonic crystal are 420 nm and 0.32. And d is varied from 110 to 1430 nm based on fabrication and epitaxial structure considerations. From simulated results, we obtain the bonding and anti-bonding states based on $WG_{6,1}$ mode and the mode profiles in electrical-field in x-z plane when $d = 440$ nm are shown in Fig. 4.4 (a) and (b). The relationship between the air-gap distance and the resonance wavelengths are shown in Fig. 4.4 (c), which can be easily analog to electronic bonding and anti-bonding states in molecules. Then we calculate their Q factors when $d = 440$ nm and obtain high Q factors from bonding ($Q_{bonding}$) and anti-bonding ($Q_{anti-bonding}$) states of 75,200 and 22,700. The former one is even higher than that of $WG_{6,1}$ mode ($Q_{original} \sim 38,000$) in original photonic crystal CD_2 microcavity. Thus, we choose the bonding state

43

and further investigate its Q factor variations with different air-gap distances from 110 to 1430 nm.

The relationship between $Q_{bonding}$ and air-gap distance d is shown in Fig. 4.5. In Fig. 4.5, at beginning, $Q_{bonding}$ is lower than $Q_{original}$ ($\sim$ 38,000, denoted by the horizontal red-line) when $d < 330$ nm. This is because when the two membranes are brought closer and closer, the individual one becomes an asymmetric structure gradually due to the presence of the other. In this case, the TE-polarized PBG effect will be broken and there will be extra modal losses due to coupling to TM-polarization [34], which dominates the Q factors over the coupling strength
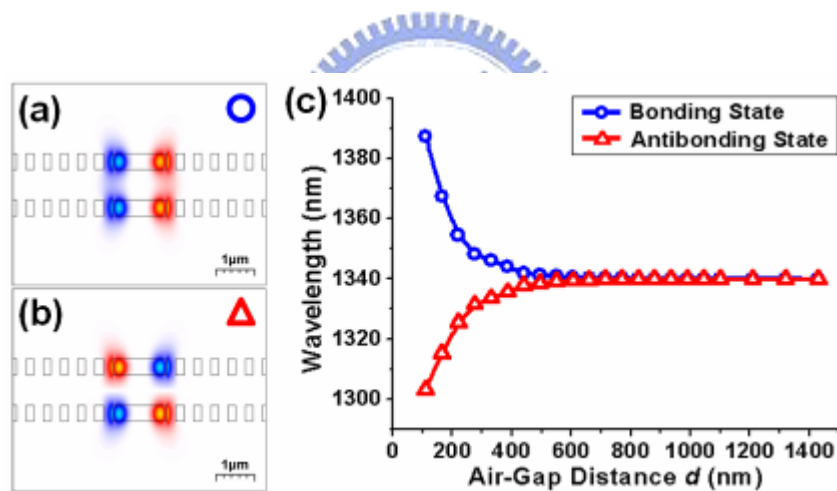
Fig. 4.4 The simulated electrical-field profiles of (a) bonding and (b) anti-bonding states in x-z plane. (c) The relationship between wavelengths and air-gap distance of bonding and anti-bonding states, which can be easily analog to electronic states in molecules.

Fig. 4.5 The relationship between $Q_{bonding}$ and air-gap distance d that is varied from 110 to 1430 nm.

between the two membranes. This also can be directly confirmed by the presence of stronger TM-polarized components in simulations. Due to this effect, we obtain over 11-fold $Q_{bonding}$ variation (from 9,700 to 107,620) within 440 nm air-gap distance variation from $d = 110$ to 550 nm (Region I in Fig. 3.5). This phenomenon is very different from the Q insensitivity in single divided membrane used for energy conservation applications [35] when d is varied within similar range. The structure we present here is very suitable for dynamic control of Q factor by controlling the PBG effect due to structural symmetry breaking when d is varied within Region I.

When d continues to increase, the losses caused by the TM-polarized coupling will be reduced and the weak-coupling effect between the two membranes will take the lead in Q factor. In Region II, we obtain a dramatic increase of $Q_{bonding}$ up to 800,000 when $d = 880$ nm, which is 21-fold enhancement compared with $Q_{original}$. Actually, the similar Q enhancement (~ 23-fold) by PM coupling in the in-plane direction is also reported in micro-disk system by

S. V. Boriskina [36]. However, unlike WG modes in micro-disk PMs in Ref. [36], the phase-shifting degenerate WG modes in photonic crystal CD_2 microcavity are greatly suppressed and with relatively low Q factors due to micro-gear effect. Thus, the bonding and anti-bonding modes here are both non-degenerate modes, which is a great feature and can avoid unnecessary parasitic noises in designing PIC applications. In Region II, we also find a relatively low $Q_{bonding}$ of 26,000 when $d = 715 - 770$ nm, which leads to over 30-fold $Q_{bonding}$ variation from 26,000 to 800,000 with almost invariant bonding state wavelength (< 0.12 nm) within 160 nm air-gap distance variation. This large $Q_{bonding}$ variation is even higher than the one in Region I.

The large $Q_{bonding}$ variations in Regions I and II both indicate an important feature of this structure design, that is, one could dynamically trap and release photons [37] in DLPMs by dynamic tuning the air-gap distance and controlling the Q factors dynamically to achieve coupling resonator optical waveguides without delay-bandwidth product limitation for slow light [38]. Most importantly, the dynamic gap-distance tuning in this double-layer structure can be achieved by micro-electro-mechanical actuator on photonic crystal membranes [39] demonstrated in optical micro-electro-mechanical system. In addition, this design with controllable coupling behavior in the vertical direction also shows the possibility of promoting the 2D planar PICs into 3D configurations.

Finally, when the air-gap distance increases to be larger than 1 μm, $Q_{bonding}$ comes closer to $Q_{original}$. This is because the coupling strength becomes very weak and the behaviors of top and bottom microcavities tend to act as two independent CD_2 microcavities.

4.3   Fabrication

4.3.1   Designed Epitaxial Structure

Considering our available dry-etching, the GaAs based material is used. The designed epitaxial structure for DLPM is shown in Fig. 4.6. The structure is formed by a 200nm GaAs single QW and a 200nm GaAs layer, which are separated by AlGaAs sacrificial layer. The measure PL spectrum is centered at 1180 nm.
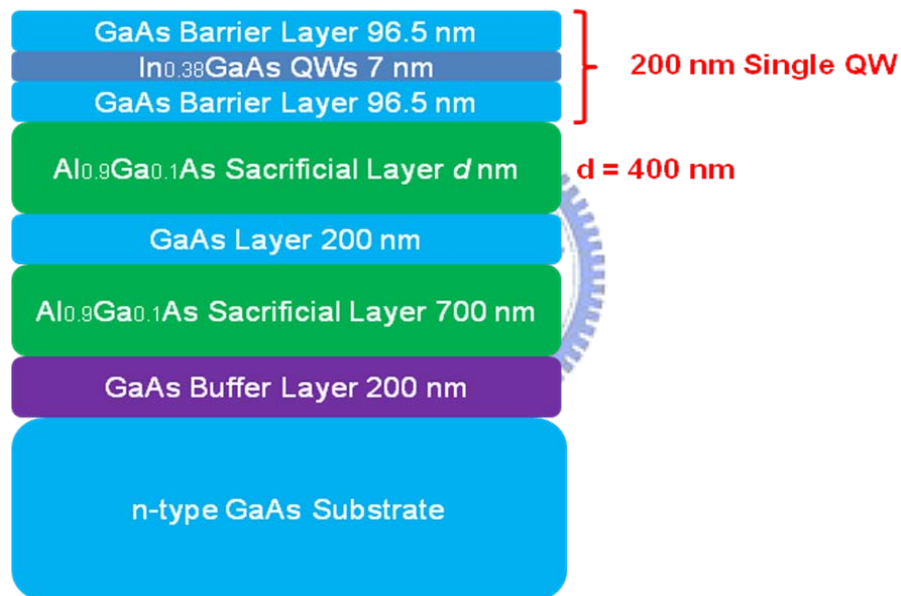
Fig. 4.6   The designed GaAs based epitaxial structure for DLPM.

After the fabrication, the two $Al_{0.9}Ga_{0.1}As$ sacrificial layers would be etched and form the double layer structure. There is only one single QW in the first layer because the second layer will not be pumped by laser diode in measurement. Here, we use the second layer just for coupling from the first one. Some fabrication process different from those in InP / InGaAsP materials will be introduced in the following paragraphs.

4.3.2   Dielectric Deposition & Pattern Definition

At first, the Si_3N_4 hard mask layer will be deposited. The thickness of Si_3N_4 is 300 nm. The reason why we choose a larger thickness than previous one is avoiding the Si_3N_4 hard breaking before achieving the depth we need. The dry-etching rate of GaAs is slowly, and we need to achieve the etching depth about 800 nm in double layer structure. The photonic crystal pattern will also be defined on PMMA layer and the designed pattern is shown in Fig. 4.7. There are two reasons why we would like to add two windows in both sides of the pattern, as shown in Fig..One reason is expand the etching range and the wet etching ratio. The other reason is supposing to observe through the large air hole that if the patterns are well etched.
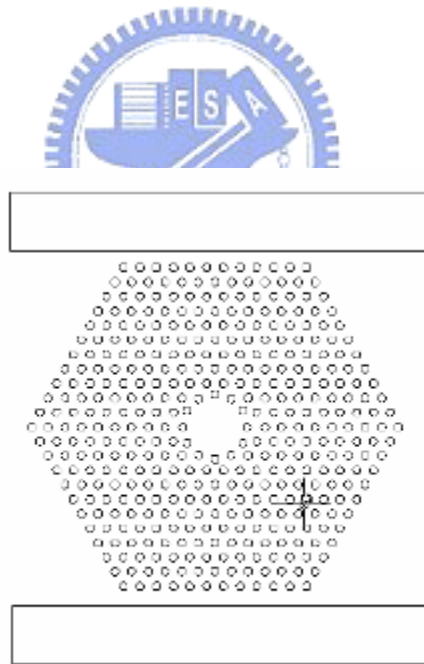
**Fig. 4.7**   The designed photonic crystal CD_2 microcavity pattern with windows.

4.3.3 Patterns Transfer

After the patterns definition by E-beam, the pattern will be transferred into Si_3N_4 layer also by RIE dry etching process. The gas flow rate of CHF_3 and O_2 are 5 sccm and 50 sccm, respectively.

And then, the double layer is etched by $H_2/CH_4/Cl_2$ mixed gases in ICP mode dry etching. The etching environment recipes are 73 W RF power, 1,000 W ICP power and 4 mTorr at 150 °C. The gas flow pressure of H_2, CH_4, and Cl_2 are 0.8, 0.4 and 0.3 mTorr, respectively. The etching rate in $H_2/CH_4/Cl_2$ mixed gas is 5.5 nm / sec on average and the selectivity etching rate to Si_3N_4 is 6.

We can observe several important factors in the patterns transferring. The first one is the dry-etching time. From Fig. we know that the etching depth will not be deep enough until the etching time is 290 seconds. Fig. 4.8 (c) shows that when the etching time is 280 seconds, the depth of the holes are not deep enough and the holes won't pass through the second GaAs layer to sacrificial layer. When etching time is increased to 300 seconds, the Si_3N_4 is not thick enough and the pattern would be broken. As results, the proper etching time for ICP is 290 seconds.
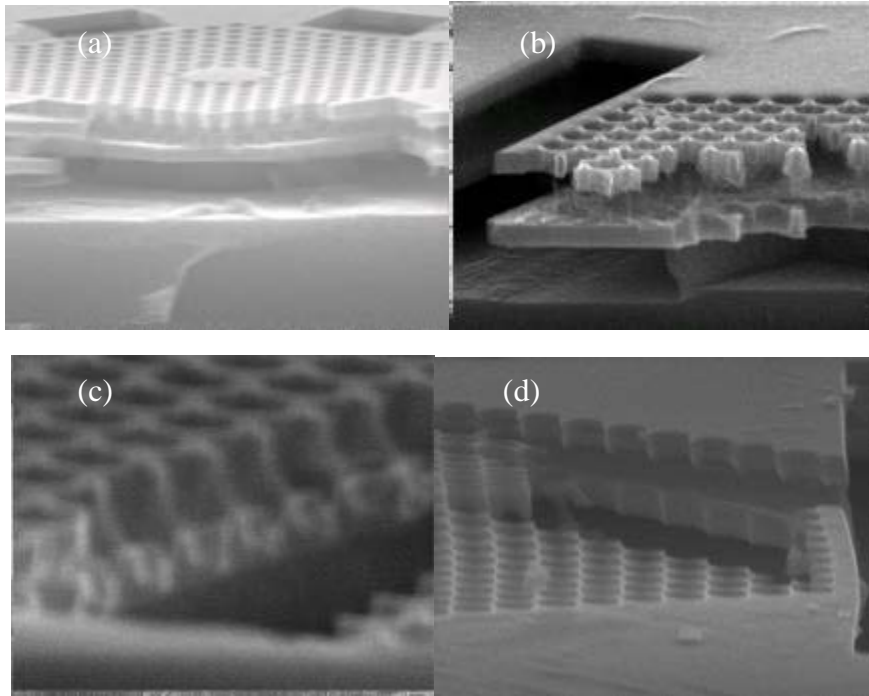
Fig. 4.8 The fabricated patterns with different etching time of (a) 180, (b) 220, (c) 280, and (d) 290 seconds. The fabricated hole radius is 122.5 nm in diameter.

The other factor is the size of air-hole, as shown in Fig. 4.9. When the radius of the holes are smaller than 109 nm in diameter, that means the *r/a* ratio is smaller than 0.32 when the lattice constant (a) is 340 nm, the etching deep will not be deeper after the etching time is increased to 220 seconds. But when the air-holes radius is increased to 122.5 nm in diameter, the holes will become deeper and deeper until passing through the second GaAs layer by 290 seconds etching time, as shown in Fig. 4.8 (d). The phenomenon tells us that we can not apply it on photonic crystal CD_2 microcavity but on 12-fold QPC D_2 microcavity since the *r/a* ratio of photonic crystal CD_2 microcavity cannot be larger than 0.3 to avoid the holes overlap. But that of 12-fold QPC D_2 microcavity can be larger than 0.3 even to 0.4. That why we use 12-fold QPC D_2 microcavity instead of photonic crystal CD_2 microcavity.
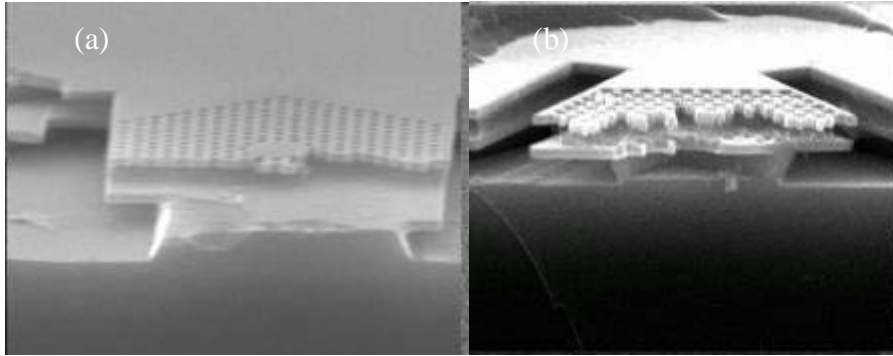
Fig. 4.9 The patterns with air-holes radius 109 nm in diameter with the dry-etching time of (a) 220 and (b) 290 seconds.

4.3.4 Substrate Undercut

Finally, the membrane structure will be constructed by selective wet-etching process by mixture solution with $H_2PO_3 : H_2O = 1 : 2$ for 60 seconds. This process also smoothes the surface and the sidewall of the air holes. This process could be also regarded as a gentle wet etching process to reduce the optical loss caused by the surface roughness.

From Fig. 4.10 (a), we can also clearly observe that the windows can help for wet etching. Fig. 4.10 (a) and (b) show that there still are residual without adding window in the same period of microcavity.
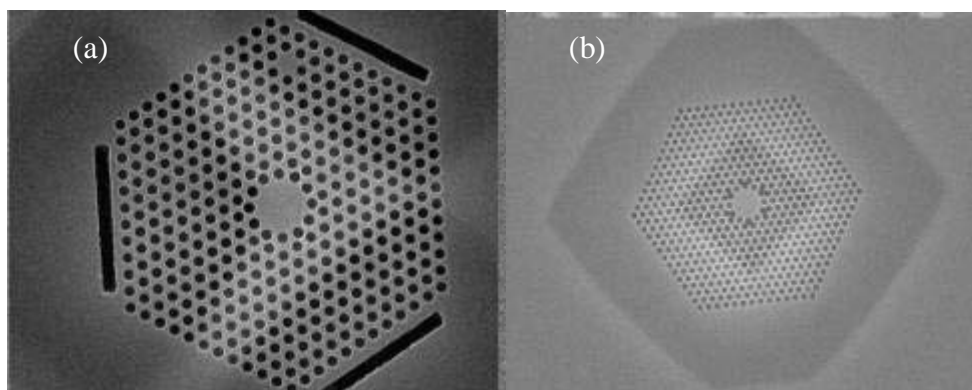
Fig. 4.10 The photonic crystal CD_2 microcavity patterns (a) with and (b) without windows

Next we will discuss the effect of etching time. We increase etching time from 30, 50, to 80 seconds, as shown in Fig. 4.11. We can clearly observe the etching range by the scheme, the patterns are not full etched until the etching time achieve 80 seconds. At this moment, the etching range is eight periods, we will not expand the etching time because too large range of etching would cause patterns bench. Besides, eight periods of DLPM is enough for providing sufficient in-plane confinement. The SEM pictures of fabricated DLPM are shown in Fig. 4.12.
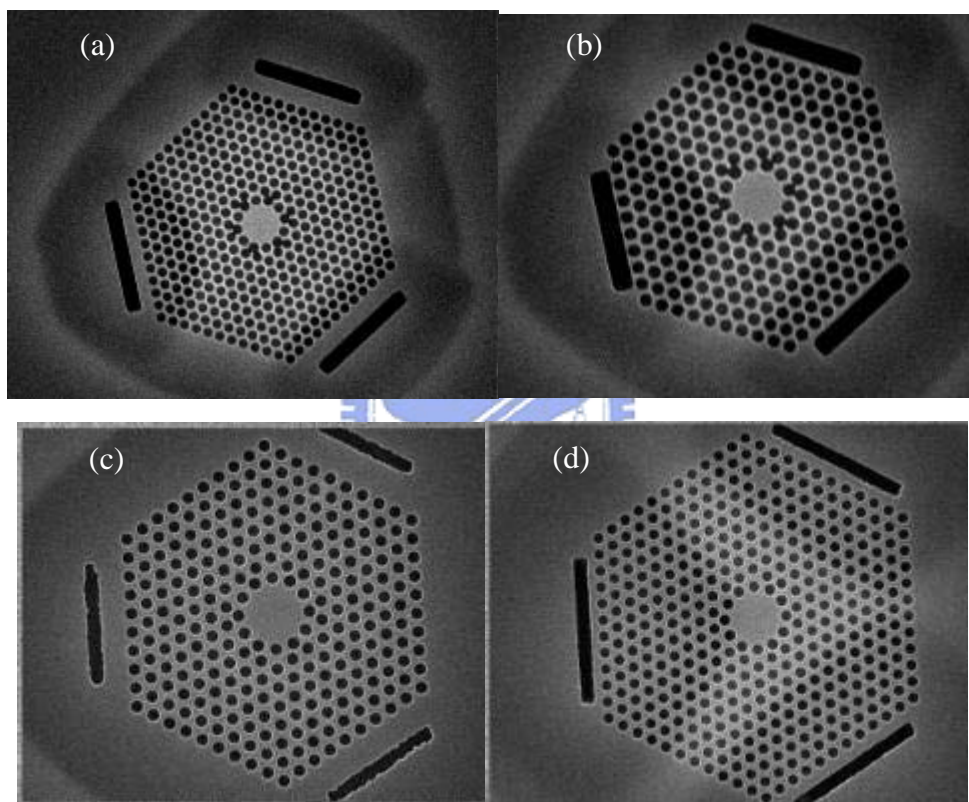
Fig. 4.11   The photonic crystal etched patterns with wet etching time and period of (a) 30 seconds and eight periods, (b) 50 seconds and eight periods, (c) 80 seconds and eight periods, and (d) 80 seconds and ten periods.
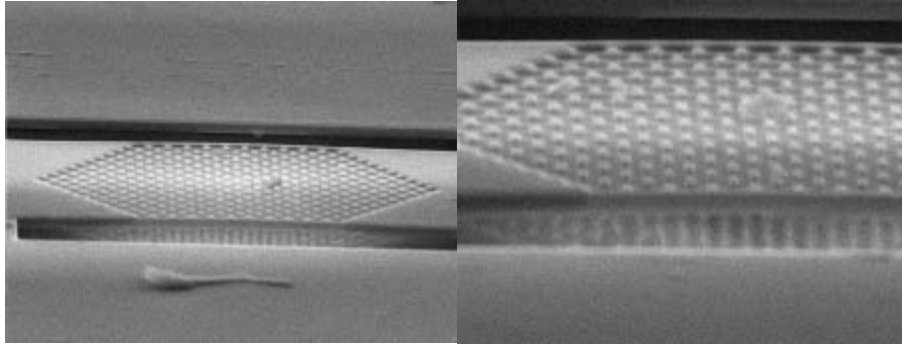
Fig. 4.12 The tilted-view SEM pictures of fabricated DLPM.

4.4 Conclusion

In this chapter, based on photonic crystal CD_2 microcavity we proposed in last chapter, we will propose a brand new vertical coupled PM based on double layer structure. By using 3D FDTD simulations, basic PM states will be addressed. By varying the gap distance from 110 to 1430 nm, we investigate the tunable PM state properties including wavelength and Q factor. We obtain a highly enhance Q factor from bonding state of 800,000 when $d = 880$ nm, which will be useful in slow-light applications. Finally, we also develop its fabrication process on GaAs based material. Some fabrication problems are addressed and solved, including stress releasing and dry-etching depth for double layer structure.

Chapter 5 Conclusions

In the first part of this thesis, in chapter 2, we have investigated basic WG modal properties in micro-disk and different topologies in micro-disk, including micro-gear and micro-flower.   In micro-gear, we obtain a 73 % enhanced Q factor of 1,170 from Q mapping by varying the grating width and height. We further optimize the micro-gear to be micro-flower by modifying the grating boundary to be curved. We also obtain 93 % enhanced Q factor of 1,310 from Q mapping by varying the grating boundary curvature. These results are also analyzed and discussed.

In chapter 3, we propose a novel photonic crystal microcavity (CD_2 microcavity) design sustaining high Q $WG_{6,1}$ mode by modifying the cavity boundary. The WG modal properties are simulated by 3D FDTD simulations. And then we apply the optimized micro-flower topology in chapter 2 on the photonic crystal CD_2 microcavity in order to increase the vertical Q factor of $WG_{6,1}$ mode. By further optimizing the curvature of micro-flower topology, we obtain the enhanced vertical Q factor of 1,000,000 from $WG_{6,1}$ mode, which is 30-fold enhancement of original Q factor (~38,000) of $WG_{6,1}$ mode. According to our design, we also fabricated the photonic crystal CD_2 microcavity with micro-flower topology with different curvatures. From the measurement results, we obtain a Q factor variation from different fabricated CD_2 microcavity with micro-flower topology with different curvatures, which agree with our simulated results.

In the second part of this thesis, in chapter 4, we have introduced photonic molecules composed by general micro-structure and photonic crystal microcavity. We also figure out the main disadvantages of photonic molecules composed by above two approaches. In order to solve these problems, we propose a brand new vertical coupling structure based on photonic

crystal CD_2 microcavity named double layer photonic molecules (DLPM). In this design, at first, we address the bonding and anti-bonding mode in the DLPM. By tuning the gap distance, we also investigate the tunable PM states properties, including Q factor and wavelength. It is worthy to note that we obtain a high Q factor of 800,000 from bonding state, which is over 30-fold enhancement. The physical mechanisms of Q variation with different gap distances are also analyzed and addressed. This design shows potential in dynamically controlling photon in slow light applications.

We also develop the related fabrication processes for this double layer structure. Due to present fabrication consideration, GaAs based material and double-layered epitaxial structure are used and designed. In the fabrication processes, several effective factors should be considered, including the process by changing patterns design, periods of the pattern, the windows for releasing stress and holes size for dry etching depth, and dry / wet etching time for device undercut.

References

1. S. L. McCall, A.F.J. Levi, R.E. Slusher, S.J. Pearton, and R. A. Logan, "Whispering-gallery mode microdisk lasers," *Appl. Phys. Lett* **60**, p.289(1992)

2. R. E. Slusher, A.F.J. Levi, U. Mohideen, S. L. McCall, S.J. Pearton, and R. A. Logan," Threshold characteristics of semiconductor microdisk lasers," *,Appl. Phys. Lett.* **63**, p.1310 (1993)

3. W. Fang, D. B. Buchholz, R. C. Bailey, J. T. Hupp, R. P. H. Chang, and H. Cao;" Detection of chemical species using ultraviolet microdisk lasers," *Appl. Phys. Lett.* **85**, p.3666 (2004)

4. P. Michler, A. Kiraz, C. Becher, W. V. Schoenfeld,P. M. Petroff, L. Zhang, E. Hu, and A. Imamoglu, *Science* **290**, p.2282(2000)

5. Y. Akahane, T. Asano, B. S. Song, and S. Noda, "High-Q photonic nanocavity in a two-dimensional photonic crystal," *Nature(London)* **425**, p.944-947

6. H. Y. Ryu, H.G. Park, and Y. H. Lee, "Two-dimensional photonic crystal Semiconductor Lasers: computational design, fabrication, and characterization," *IEEE J. Sel. Top. Quantum Electron.* **vol.8**, p.891-908 (2002)

7. Masayuki Fujita and Toshihiko BaBa, "Microgear laser," *Appl.Phys.***vol.80** No.12,p.2051 (2001)

8. Hwang, J.K.; Ryu, H.Y.; Song, D.S.; Han, I.Y.; Park, H.K.; Jang, D.H.; Lee, Y.H. ;" Continuous room-temperature operation of optically pumped two-dimensional photonic crystal lasers at 1.6 mu/m," *IEEE Photonics Technology Letter*, **vol. 12**, NO. 10, Oct. 2000

9. Hong-Gyu Park; Jeong-Ki Hwang; Joon Huh; Han-Youl Ryu; Se-Heon Kim; Jeong-Soo Kim; Yong-Hee Lee; "Characteristics of modified single-defect two-dimensional photonic crystal lasers," *IEEE Journal of Quantum Electronics*, **vol. 38**, NO. 10, Oct. 2002

10. E. Yablonovitch, "Inhibited Spontaneous Emission in Solid-State Physics and Electronics," *Phys. Rev. Lett.*, **vol58(20)**,p.2059-2062, (1987)

11. R. K. Lee, O. J. Painter, B. D'Urso, A. Scherer, and A. Yariv," Measurement of spontaneous emission from a two-dimensional photonic band gap defined microcavity at near-infrared wavelengths," *Appl. Phys. Lett.* **74**, p.1522 (1999)

12. Andrei Faraon, Edo Waks, Dirk Englund, Ilya Fushman, and Jelena Vučković," Efficient photonic crystal cavity-waveguide couplers," *Appl. Phys. Lett.* **90**, 073102 (2007)

13. Hong-Gyu Park, Jeong-Ki Hwang, Joon Huh, Han-Youl Ryu, Se-Heon Kim, Jeong-Soo Kim, and Tong-Hee Lee," Characteristics of Modified Single-Defect Two-Dimensional Photonic crystal Laser," *IEEE Jour. of Quantum Electronics*, **vol.38**, No.10, October

2002

14. Atsuo Nakagawa, Satoru Ishii, and Toshihiko BaBa"Photonic molecule laser composed of GaInAsP microdisks," *Appl. Phys. Lett*. **86**, 041112 (2005)

15. S. Ishii, A. Nakagawa and Toshihiko BaBa, "Modal-Characteristics and Bistability inTwin Microdisk Photonic Molecule Laser," *IEEE J. Sel. Topics Quantum Electron*.**vol.12**, p.71-77 (2006)

16. S. Ishii and Toshihiko BaBa, "Bistable lasing in twin microdisk photonic molecules," *Appl.phys. Lett.* **87**, p.181102 (2005)

17. O.Painter, R.K Lee, A. Scherer, A.Yariv, J. D.O'Brien, P.D.Dapkus, and I. Kim, "Two-dimensional photonic band-gap defect mode laser," *Science* **284**, p.1819-1821 (1999)

18. H. G. Park, J. K. Hwang, J. Huh, H. Y. Ryu, S .H. Kim, J. S. Kim, and Y. H. Lee, "Characteristics of modified single defect two-dimensional photonic crystal lasers," *IEEE J. Quantum Electron*. **38**, p.1353-1365 (2002)

19. Y. Akahane, T. Asano, B. S. Song, and S. Noda, "Fine-tuned high-Q photonic crystal nanocavity," *Opt. Express*, **vol.13**, p.1202-1214 (2005)

20. K. Nozaki, S. Kita, and T. Baba, "Room temperature continuous wave operation and controlled spontaneous emission in ultrasmall photonic crystal nanolaser," *Opt. Express* **15**, p.7506-7514 (2007)

21. P. T. Lee, T. W. Lu, C. M. Yu, and C. C. Tseng, "Photonic crystal circular-shaped microcavity and its uniform cavity-waveguide coupling property due to presence of whispering gallery mode," *Opt. Express* **15**, p.9450-9457 (2007).

22. M. D. Barnes, S. M. Mahurin, A. Mehta, B. G. Sumpter, and D. W. Noid, "Three-dimensional photonic "molecules" from sequentially attached polymer-blend microparticles," *Phys. Rev. Lett*. **88**, 015508 (2002).

23. M. Bayer, T. Gutbrod, J. P. Reithmaier, and A. Forchel, "Optical Modes in Photonic Molecules," *Phys. Rev. Lett.* **81**, p.2582-2585 (1998).

24. T. Mukaiyama, K. Takeda, H. Miyazaki, Y. Jimba, and M. K. Gonokami, **"**Optical Demonstration of a Crystal Band Structure Formation,**"** *Phys. Rev. Lett.* **83**, p.5374-5377 (1999).

25. A. Nakagawa, S. Ishii, and T. Baba, "Photonic molecule laser composed of GaInAsP microdisks," *Appl. Phys. Lett.* **86**, 041112 (2005).

26. S. Ishii, A. Nakagawa, and T. Baba, "Modal Charactristics and Bistability in Twin Microdisk Photonic Molecule Lasers," *IEEE J. Sel. Topics Quantum Electron.* **12**, p.71-77 (2006).

27. S. Ishii and T. Baba, "Bistable lasing in twin microdisk photonic molecules," *Appl. Phys. Lett*. **87**, 181102 (2005).

28. O. Painter, R. K. Lee, A. Scherer, A. Yariv, J. D. O'Brien, P. D. Dapkus, and I. Kim,

"Two-Dimensional Photonic Band-Gap Defect Mode Laser," *Science* **284**, p.1819-1821 (1999).

29. H. G. Park, J. K. Hwang, J. Huh, H. Y. Ryu, S. H. Kim, J. S. Kim, and Y. H. Lee, "Characteristics of Modified Single-Defect Two-Dimensional Photonic Crystal Lasers," *IEEE J. Quantum Electron*. **38**, p.1353-1365 (2002).

30. Y. Akahane, T. Asano, B. S. Song, and S. Noda, "Fine-tuned high-Q photonic-crystal nanocavity," *Opt. Express*, **13**, p.1202-1214 (2005).

31. K. Nozaki, S. Kita, and T. Baba, "Room temperature continuous wave operation and controlled spontaneous emission in ultrasmall photonic crystal nanolaser," *Opt. Express* **15**, p.7506-7514 (2007).

32. S. Ishii, K. Nozaki, and T. Baba, "Photonic Molecules in Photonic Crystals," *Jpn. J. Appl. Phys.* **45**, p.6108-6111 (2006).

33. D. O'Brien, M. D. Settle, T. Karle, A Michaeli, M. Salib, and T. F. Krauss, "Coupled photonic heterostructure nanocavities," *Opt. Express* **15**, p.1228-1233 (2007).

34. M. Notomi, H. Taniyama, S. Mitsugi, and E. Kuramochi, "Optomechanical Wavelength and Energy Conservation in High-Q Double-Layer Cavities of Photonic Crystal Slabs," *Phys. Rev. Lett*. **97**, 023903 (2006).

35. Y. Tanaka, T. Asano, Y. Akahane, B. S. Song, and S. Noda, "Theoretical investigation of a two-dimensional photonic crystal slab with truncated cone air holes," *Appl. Phys. Lett.* **82**, p.1661-1663 (2003).

36. S. V. Boriskina, "Theoretical prediction of dramatic Q-factor enhancement and degeneracy removal of whispering gallery modes in symmetrical photonic molecules," *Opt. Lett.* **31**, p.338-340 (2006).

37. T. Tannabe, M. Notomi, E. Kuramochi, A. Shinya, and H. Taniyama, "Trapping and delaying photons for one nanosecond in an ultrasmall high-Q photonic-crystal nanocavity," *Nature Photon*. **1**, p.49-52 (2007).

38. M. F. Yanik and S. Fan, "Stopping Light All Optically," *Phys. Rev. Lett*. **92**, 083901 (2004).

39. Y. Kanamori, T. Kitani, and K. Hane, "Control of guided resonance in a photonic crystal slab using microelectromechanical actuators," *Appl. Phys. Lett*. **90**, 031911 (2007).

Vita

Meng-Ying Lin was born on 13 June, 1984 in Taipei City, Taiwan. She received the B.S. degree from Department of Engineering and System Science, National Tsing Hua University, Hsinchu, Taiwan in 2006. The M.S. degree will be received from Department of Photonics and Institute of Electro-Optical Engineering, National Chiao Tung University, Hsinchu, Taiwan in 2008. Her researches include photonic crystal microcavity and photonic molecules.